

Extracting kinetic freeze-out temperature and radial flow velocity from an improved Tsallis distribution

Hai-Ling Lao^a, Fu-Hu Liu^{a,1}, and Roy A. Lacey^b

^a*Institute of Theoretical Physics, Shanxi University, Taiyuan, Shanxi 030006, China*

^b*Departments of Chemistry & Physics, Stony Brook University, Stony Brook, NY 11794, USA*

Abstract: We analyze the transverse momentum (p_T) spectra of identified particles (π^\pm , K^\pm , p , and \bar{p}) produced in gold-gold (Au-Au) and lead-lead (Pb-Pb) collisions over a $\sqrt{s_{NN}}$ (center-of-mass energy per nucleon pair) range from 14.5 GeV [one of the Relativistic Heavy Ion Collider (RHIC) energies] to 2.76 TeV [one of the Large Hadron Collider (LHC) energies]. For the spectra with a narrow p_T range, an improved Tsallis distribution which is in fact the Tsallis distribution with radial flow is used. For the spectra with a wide p_T range, a superposition of the improved Tsallis distribution and an inverse power-law is used. Both the extracted kinetic freeze-out temperature (T_0) and radial flow velocity (β_T) increase with the increase of $\sqrt{s_{NN}}$, which indicates a higher excitation and larger expansion of the interesting system at the LHC. Both the values of T_0 and β_T in central collisions are slightly larger than those in peripheral collisions, and they are independent of isospin and slightly dependent on mass.

Keywords: Improved Tsallis distribution, kinetic freeze-out temperature, radial flow velocity

PACS: 25.75.-q, 25.75.Ag, 25.75.Ld, 24.10.Pa

1 Introduction

Transverse momentum (p_T) spectra of identified particles produced in proton-proton, proton-nucleus, and nucleus-nucleus collisions at high energies are important quantities measured in experiments. In particular, gold-gold (Au-Au) collisions at the Relativistic Heavy Ion Collider (RHIC) and lead-lead (Pb-Pb) collisions at the Large Hadron Collider (LHC) and other high energy nucleus-nucleus collisions have been providing us excellent chances to study the signals and features of quark-gluon plasma (QGP), the properties of multi-particle production, and the characteristics of the interesting system. In the study of p_T spectra, we can obtain some useful information which contains, but is not limited to, the effective temperatures (T) when the interacting system emit different particles, chemical freeze-out temperature (T_{ch}) based on particle ratios, kinetic freeze-out temperature (T_0), and transverse or radial flow velocity (β_T).

On the extraction of T , one can use different functions or distribution laws such as the standard (Boltzmann, Fermi-Dirac, or Bose-Einstein) distribution [1–4], the Tsallis distribution [4–10], and others. On the extraction of T_{ch} , one can use the particle ratios due to different normalization constants for different identified particle spectra in a given p_T range. On the extractions of T_0 and β_T , one can use the distributions which contains simultaneously T_0 and β_T such as the blast-wave model [11, 12] and an improved Tsallis distribution (the Tsallis distribution with radial flow) [13, 14], as well as

an alternative method which is used in our recent works [15–17] and partly used in the previous literature [11, 18–20].

The blast-wave model [11, 12] is a traditional and current method which has wide applications. This model makes the simple assumption that particles are locally thermalized in a hard-sphere uniform density source at a kinetic freeze-out temperature and are moving with a common collective transverse radial flow velocity field. The improved Tsallis distribution is a new method which is suggested by Sahoo and his colleagues [13, 14] and has a few applications. This model is based on the Tsallis distribution and introduces radial flow in it. Thus, the temperature parameter in the improved Tsallis distribution is the kinetic freeze-out temperature T_0 . We are curious to use the improved Tsallis distribution in the present work to obtain some distinctive conclusions. The alternative method is partly a new one, in which the extraction of T_0 has some applications [11, 18–20]. In the alternative method, T_0 is regarded as the intercept in the linear relation between T and m_0 , and β_T is regarded as the slope in the linear relation between $\langle p_T \rangle$ and $\langle m \rangle$, where m_0 , $\langle m \rangle$, and $\langle p_T \rangle$ denote the rest mass, mean moving mass, and mean p_T , respectively.

We are interested in the consistency and differences of the three methods in their results. In fact, their differences are larger than their consistency. The blast-wave model [11, 12] and the improved Tsallis distribution [13, 14] have their assumptions and pictures respectively. The alternative method itself is independent of mod-

¹E-mail: fuhuliu@163.com; fuhuliu@sxu.edu.cn

els, though its result T_0 depends on T which depends on distribution laws of p_T , and its result β_T is independent of distributions due to the same $\langle p_T \rangle$ and $\langle m \rangle$ for given experimental spectra. Generally, the Tsallis distribution results in lower T and T_0 than the standard distribution. Also, the blast-wave model [11, 12] and the improved Tsallis distribution [13, 14] result in lower T_0 than the alternative method when using the standard distribution. Different distributions are in fact different ‘thermometers’ or ‘thermometric scales’ and ‘speedometers’.

In this paper, we shall use the improved Tsallis distribution [13, 14] to fit p_T spectra of identified particles (π^\pm , K^\pm , p , and \bar{p}) produced in Au-Au collisions at the RHIC and Pb-Pb collisions at the LHC. The center-of-mass energy per nucleon pair, $\sqrt{s_{NN}}$, considered by us is from 14.5 GeV to 2.76 TeV. After fitting the experimental data measured by the STAR [21, 22], PHENIX [20, 23–28], and ALICE Collaborations [29], we analyze the tendency of parameters.

The rest part of this paper is structured as follows. A brief description of the formalism is presented in section 2. Results on comparisons with experimental data and discussion are given in section 3. Finally, we summarize our main observations and conclusions in section 4.

2 The formalism

High energy collisions are a complex process in which many emission sources are formed. The sources with the same excitation degree may form a local equilibrium state which can be described by the standard distribution. For different equilibrium states which have different excitation degrees, different temperature parameters may be used. Generally, a two- or three-component standard distribution can describe the p_T spectrum in a not too wide p_T range, which reflects the temperature fluctuation of the interacting system. At the same time, a two- or three-component standard distribution can be described by the Tsallis distribution with the parameters which contains mainly T and the entropy index q .

The Tsallis distribution, i.e. the p_T distribution in the Tsallis statistics, has more than one forms. In a recent work [10], five forms of Tsallis and related distributions are collected. We have the Tsallis distribution at mid-rapidity ($y \approx 0$) as follows

$$f_1(p_T) = C_1 p_T m_T \left[1 + (q-1) \frac{m_T}{T} \right]^{-q/(q-1)}, \quad (1)$$

where C_1 is the normalization constant which results in $\int_0^\infty f_1(p_T) dp_T = 1$, $m_T = \sqrt{p_T^2 + m_0^2}$ is the transverse mass, and m_0 is the rest mass. The chemical potential is not included in Eq. (1) due to its small effect on the p_T distribution. Other four Tsallis-related distributions

at mid-rapidity are

$$f_2(p_T) = C_2 p_T m_T \left[1 + (q-1) \frac{m_T}{T} \right]^{-1/(q-1)}, \quad (2)$$

$$f_3(p_T) = C_3 p_T \left[1 + (q-1) \frac{m_T}{T} \right]^{-q/(q-1)}, \quad (3)$$

$$f_4(p_T) = C_4 p_T \left[1 + (q-1) \frac{m_T}{T} \right]^{-1/(q-1)}, \quad (4)$$

and

$$f_5(p_T) = C_5 p_T \left[1 + \frac{q-1}{T} (m_T - m_0) \right]^{-1/(q-1)}, \quad (5)$$

where $C_{2,3,4,5}$ denote the different normalized constants which result respectively in $\int_0^\infty f_{2,3,4,5}(p_T) dp_T = 1$ for different distribution forms which are rearranged comparing with ref. [10]. Although we have used the same symbols, the values of T (or q) in Eqs. (1)–(5) are different from each other.

The above Tsallis-related distributions can be used to describe the p_T spectra of particles produced in soft excitation process which occurs between gluons and/or sea quarks and contributes to a not too wide p_T range. Because of their similarity, one of them is enough for the description of soft process. From the similarity and self-consistency to the standard distribution, Eqs. (1) and (3) are the favorable choices. However, the values of T obtained from the Tsallis-related distributions are only effective temperatures which contain the contributions of thermal motion and flow effect together. To disentangle the thermal motion and flow effect, an alternative method can be used in the case of analyzing p_T spectra of identified particles.

Fortunately, Sahoo and his colleagues [13, 14] have introduced the radial flow velocity to the Tsallis distribution Eq. (1). According to ref. [13], to include the radial flow in a relativistic scenario, the Tsallis distribution function has been expanded in a Taylor series in view of $(q-1)$ being very small. The normalized functional form of the distribution up to first order in $(q-1)$

is given by

$$\begin{aligned}
f_S(p_T) = C_0 & \left\{ 2T_0[rI_0(s)K_1(r) - sI_1(s)K_0(r)] \right. \\
& - (q-1)T_0r^2I_0(s)[K_0(r) + K_2(r)] \\
& + 4(q-1)T_0rsI_1(s)K_1(r) \\
& - (q-1)T_0s^2K_0(r)[I_0(s) + I_2(s)] \\
& + \frac{(q-1)}{4}T_0r^3I_0(s)[K_3(r) + 3K_1(r)] \\
& - \frac{3(q-1)}{2}T_0r^2s[K_2(r) + K_0(r)]I_1(s) \\
& + \frac{3(q-1)}{2}T_0s^2r[I_0(s) + I_2(s)]K_1(r) \\
& \left. - \frac{(q-1)}{4}T_0s^3[I_3(s) + 3I_1(s)]K_0(r) \right\}, \quad (6)
\end{aligned}$$

where C_0 is the normalized constant which results in $\int_0^\infty f_S(p_T)dp_T = 1$, $r \equiv \gamma m_T/T_0$, $s \equiv \gamma\beta_T p_T/T_0$, $\gamma = 1/\sqrt{1-\beta_T^2}$, and $I_n(s)$ and $K_n(r)$ are the modified Bessel functions of the first and second kinds, respectively. We call Eq. (6) the improved Tsallis distribution, which is in fact the Tsallis distribution with radial flow, in which there are three free parameters involved namely T_0 , q , and β_T .

In most cases, the p_T spectra are given in a wide p_T range. The improved Tsallis distribution, Eq. (6), is not enough to give a good description. That is, the contribution of the hard scattering process which occurs between valence quarks has to be considered. We can use the inverse power-law

$$f_H(p_T) = Ap_T \left(1 + \frac{p_T}{p_0} \right)^{-n}, \quad (7)$$

to describe the contribution of the hard scattering process, where p_0 and n are free parameters, and A is the normalized constant which depends on p_0 and n and results in $\int_0^\infty f_H(p_T)dp_T = 1$. Eq. (7) results from the QCD (quantum chromodynamics) calculus [30–32]. To describe the p_T spectra in a wide p_T range, we can use a superposition of the improved Tsallis distribution which describes the contribution of the soft excitation process and the inverse power-law which describes the contribution of the hard scattering process

$$f_0(p_T) = kf_S(p_T) + (1-k)f_H(p_T), \quad (8)$$

where k denotes the contribution ratio (relative contribution or fraction) of the improved Tsallis distribution and results naturally in $\int_0^\infty f_0(p_T)dp_T = 1$.

It should be noted that the above formalism describes the soft component using the Tsallis distribution taking into account flow in an approximate manner. For the hard component, only the power-law distribution is used. We do not need to modify the distribution for

the hard component when taking into account the flow due to the hard component being contributed from hard scattering in the early stages of the collision when the flow is not yet appearing. Comparatively, the soft component is contributed from the soft excitation in the middle and later stages of the collision when the flow is already appearing. Although both the soft and hard components are power-law distributions and they have a similar mathematical form before taking into account the flow for the soft component, the definitive final descriptions of the two components have different forms.

3 Results and discussion

Figure 1 presents the transverse momentum spectra, $(1/N_{EV})(2\pi p_T)^{-1}d^2N/(dydp_T)$, of (a)-(c) π^+ , K^+ , and p , as well as (b) π^- , K^- , and \bar{p} produced in (a)-(b) 0–5% and (c) 70–80% Au-Au collisions at $\sqrt{s_{NN}} = 14.5$ GeV, where N_{EV} on the vertical axis denotes the number of events, which means the mentioned quantity $[(2\pi p_T)^{-1}d^2N/(dydp_T)]$ per event and is usually omitted in most cases, and N denotes the number of particles. The symbols represent the experimental data of the STAR Collaboration measured in the rapidity range $|y| < 0.1$ [21]. The solid curves are our results calculated by using the improved Tsallis distribution [13, 14]. The values of free parameters T_0 , q , and β_T , normalization constant N_0 which is used to fit the data, and χ^2 per degree of freedom (χ^2/dof) are listed in Table 1. One can see that the improved Tsallis distribution describes the p_T spectra of identified particles produced in central (0–5%) and peripheral (70–80%) Au-Au collisions at $\sqrt{s_{NN}} = 14.5$ GeV.

Figure 2 is the same as Figure 1, but it shows the spectra, $(2\pi p_T)^{-1}d^2N/(dydp_T)$, for (a)-(c) π^+ , K^+ , and p , as well as (b)-(d) π^- , K^- , and \bar{p} produced in (a)-(b) 0–5% and (c)-(d) 70–80% Au-Au collisions at $\sqrt{s_{NN}} = 62.4$ GeV. The experimental data of the STAR Collaboration are taken from ref. [22]. One can see that the improved Tsallis distribution describes the p_T spectra of identified particles produced in central (0–5%) and peripheral (70–80%) Au-Au collisions at $\sqrt{s_{NN}} = 62.4$ GeV.

In Figure 3, the transverse momentum spectra of (a)-(c) π^+ , K^+ , and p , as well as (b)-(d) π^- , K^- , and \bar{p} produced in (a)-(b) 0–5% and (c)-(d) 60–92% Au-Au collisions at $\sqrt{s_{NN}} = 130$ GeV are given. The symbols represent the experimental data of the PHENIX Collaboration measured in the pseudorapidity range $|\eta| < 0.35$ [23, 24] and scaled by different amounts shown in the panels. The solid, dotted, and dashed curves are our results calculated by using the improved Tsallis distribution [13, 14], the inverse power-law [30–32], and their superposition, respectively. The values of free parameters T_0 , q , β_T , k , p_0 , and n , normalization constant N_0 , and

χ^2/dof are listed in Table 2. One can see that in most cases the superposition of the improved Tsallis distribution and the inverse power-law describes the p_T spectra of identified particles produced in central (0–5%) and peripheral (60–92%) Au-Au collisions at $\sqrt{s_{NN}} = 130$ GeV.

The situation of Figure 4 is the same as Figure 3, but it shows the spectra for (a)-(c) π^+ , K^+ , and p , as well as (b)-(d) π^- , K^- , and \bar{p} produced in (a)-(b) 0–5% and (c)-(d) 80–92% Au-Au collisions at $\sqrt{s_{NN}} = 200$ GeV. The experimental data of the PHENIX Collaboration are taken from refs. [18, 25–28]. One can see again that the superposition of the improved Tsallis distribution and the inverse power-law describes the p_T spectra of identified particles produced in central (0–5%) and peripheral (80–92%) Au-Au collisions at $\sqrt{s_{NN}} = 200$ GeV.

The situation of Figure 5 is also the same as Figure 3, but it shows the spectra for (a)-(c) π^+ , K^+ , and p , as well as (b)-(d) π^- , K^- , and \bar{p} produced in (a)-(b) 5–10% and (c)-(d) 60–92% Au-Au collisions at $\sqrt{s_{NN}} = 200$ GeV. The experimental data of the PHENIX Collaboration are taken from refs. [18, 25–28]. Once more the superposition of the improved Tsallis distribution and the inverse power-law describes the p_T spectra of identified particles produced in central (5–10%) and peripheral (60–92%) Au-Au collisions at $\sqrt{s_{NN}} = 200$ GeV.

Figure 6 is the same as Figure 3, but it shows the spectra for $\pi^+ + \pi^-$, $K^+ + K^-$, and $p + \bar{p}$ produced in (a) 0–5% and (b) 60–80% Pb-Pb collisions at $\sqrt{s_{NN}} = 2.76$ TeV. The experimental data of the ALICE Collaboration are taken from ref. [29] and measured in $|\eta| < 0.8$ for high p_T region and $|y| < 0.5$ for low p_T region. Indeed, the superposition of the improved Tsallis distribution and the inverse power-law describes the p_T spectra of identified particles produced in central (0–5%) and peripheral (60–80%) Pb-Pb collisions at $\sqrt{s_{NN}} = 2.76$ TeV.

To study the changing tendencies of parameters, Figure 7 shows the dependences of T_0 on $\sqrt{s_{NN}}$ for (a)-(c) positively and (b)-(d) negatively charged particles in (a)-(b) central and (c)-(d) peripheral Au-Au collisions at different energies, as well as for charged particles in (a)-(b) central and (c)-(d) peripheral Pb-Pb collisions at 2.76 TeV. The symbols represent T_0 extracted from different spectra for different particles in different collisions listed in Tables 1 and 2 and shown in the panels. The dashed, solid, and dotted curves are our results fitted by using the method of least squares for charged pions, kaons, and protons (antiprotons), respectively. These curves are described by the function

$$T_0 = a(\sqrt{s_{NN}})^b + c, \quad (9)$$

where the values of parameters a , b , and c , as well as χ^2/dof are given in Table 3. One can see that T_0 in-

creases with the increase of $\sqrt{s_{NN}}$, the function describes the tendency of T_0 in most cases.

The dependence of T_0 on $\sqrt{s_{NN}}$ obtained in the present work is inconsistent with the original blast-wave model [11, 12, 20, 22] which gives a lower T_0 at higher energy. Although the lower T_0 can be explained to a longer lifetime of the hot and dense QGP, the higher T_0 can be explained to a higher excitation degree. The present work extracted a higher T_0 in central collisions than in peripheral collisions, which is consistent with the improved blast-wave model [33] which uses sources of particle emission from a Tsallis distribution, and inconsistent with the original blast-wave model [11, 12, 20, 22] which uses sources of particle emission from a Boltzmann distribution. This difference can be also explained by the higher excitation degree or longer lifetime, or different ‘thermometers’ or ‘thermometric scales’ being used. From Figure 7, one can also see the slight differences for different particles in some cases. This confirms the mass-dependent differential kinetic freeze-out scenario [14, 16].

Figures 8–14 are the same as Figure 7, but they show the dependences of q , β_T , p_0 , n , k , kN_0 , and N_0 on $\sqrt{s_{NN}}$, respectively, where the product kN_0 in Figure 13 represents the yield of soft excitation process. The horizontal dashed, solid, and dotted lines in Figure 8 (or Figure 12) represent the mean values of q (or k) over different energies for charged pions, kaons, and protons (antiprotons), respectively. The dashed, solid, and dotted curves are our results fitted by using the method of least squares for charged pions, kaons, and protons (antiprotons), respectively, though some curves do not describe the tendencies of parameters. The function for the curves in Figures 8–12 is

$$Y = a + b \ln(\sqrt{s_{NN}}), \quad (10)$$

where $Y = q$, β_T , p_0 , n , or k . The function for the curves in Figures 13 and 14 is

$$Y = \exp[a + b \ln(\sqrt{s_{NN}})], \quad (11)$$

where $Y = kN_0$ or N_0 . The values of parameters a and b , as well as χ^2/dof are given in Table 4. One can see that with the increase of $\sqrt{s_{NN}}$, q and β_T increase slightly, p_0 and k decrease slightly, n , kN_0 , and N_0 increase generally. The functions describe the tendencies of parameters in some cases, while in other cases the functions fail to describe the tendencies.

The parameter q increases slightly with the increase of $\sqrt{s_{NN}}$, but the dependence of q on $\sqrt{s_{NN}}$ is not obvious. As the entropy index, q describes the degree departing from the equilibrium state or the degree of non-equilibrium. The parameters q in central and peripheral collisions are very small, which means that the two types of collisions are in the nearly equilibrium state respectively, though a slightly larger q seems to be observed

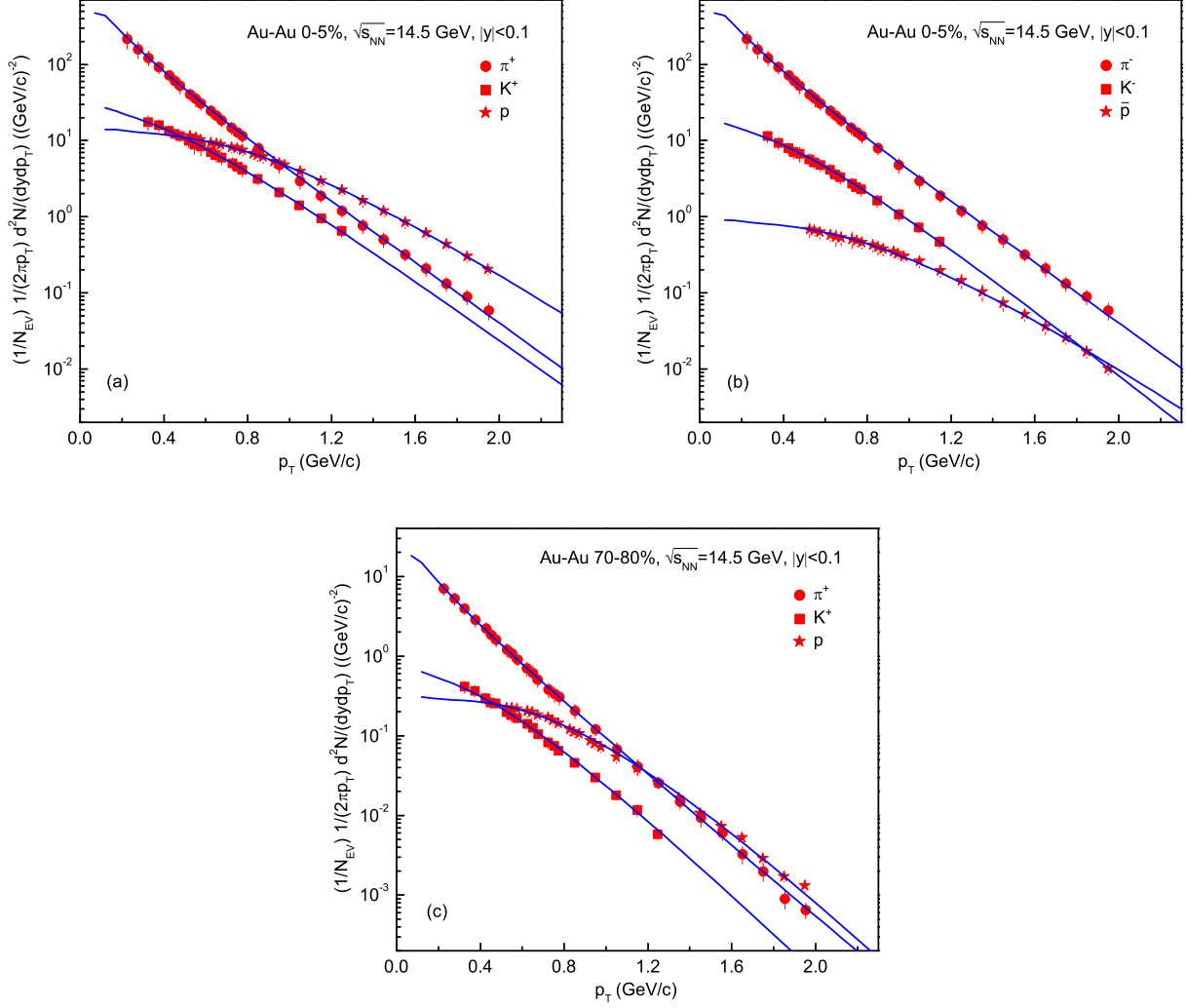


Fig. 1. Transverse momentum spectra of (a)-(c) π^+ , K^+ , and p , as well as (b) π^- , K^- , and \bar{p} produced in (a)-(b) 0–5% and (c) 70–80% Au-Au collisions at $\sqrt{s_{NN}} = 14.5$ GeV, where N_{EV} on the vertical axis denotes the number of events, which is usually omitted. The symbols represent the experimental data of the STAR Collaboration measured in the rapidity range $|y| < 0.1$ [21]. The solid curves are our results calculated by using the improved Tsallis distribution [13, 14].

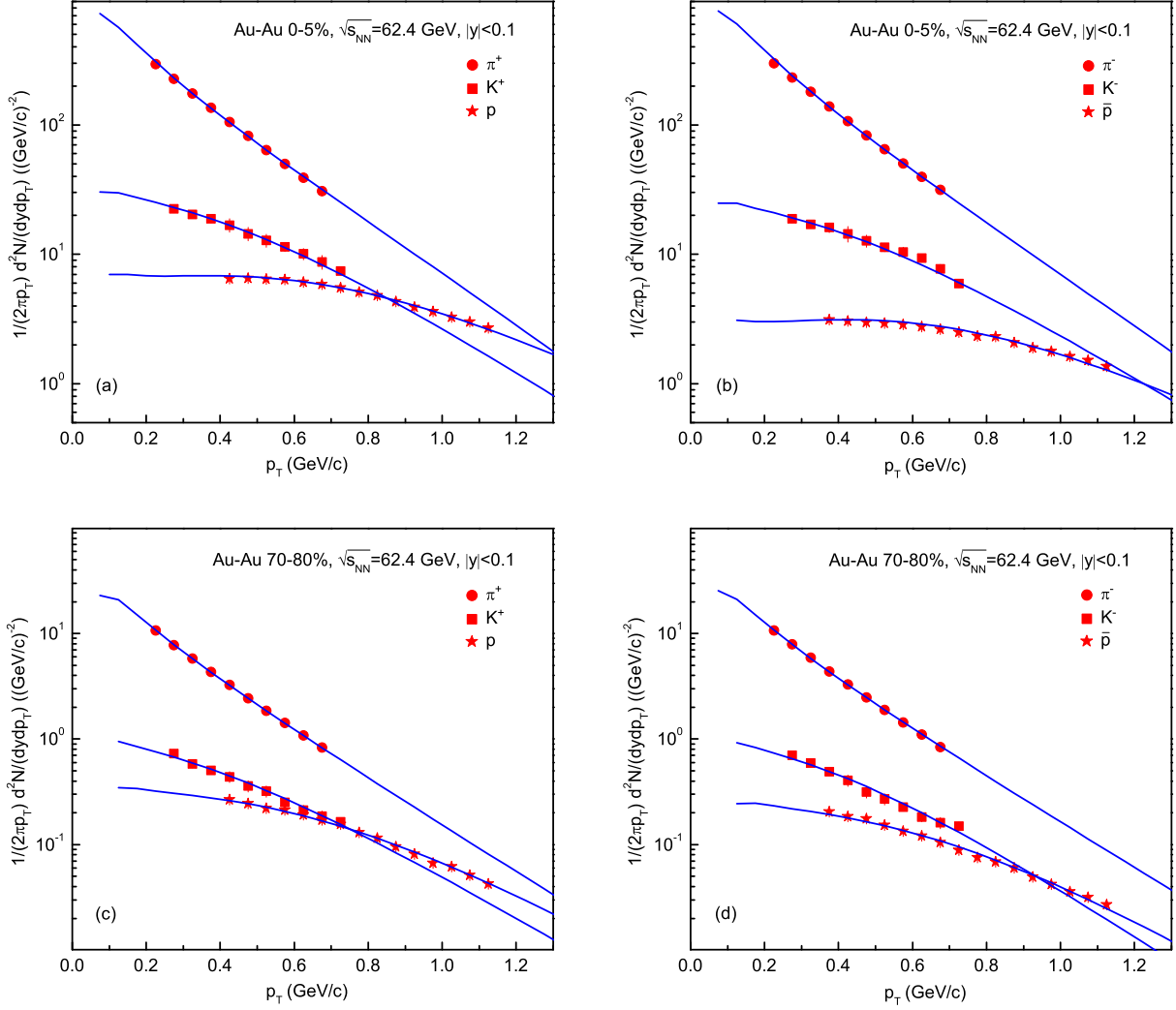


Fig. 2. Same as Figure 1, but showing the spectra for (a)-(c) π^+ , K^+ , and p , as well as (b)-(d) π^- , K^- , and \bar{p} produced in (a)-(b) 0–5% and (c)-(d) 70–80% Au-Au collisions at $\sqrt{s_{NN}} = 62.4$ GeV. The experimental data of the STAR Collaboration are taken from ref. [22].

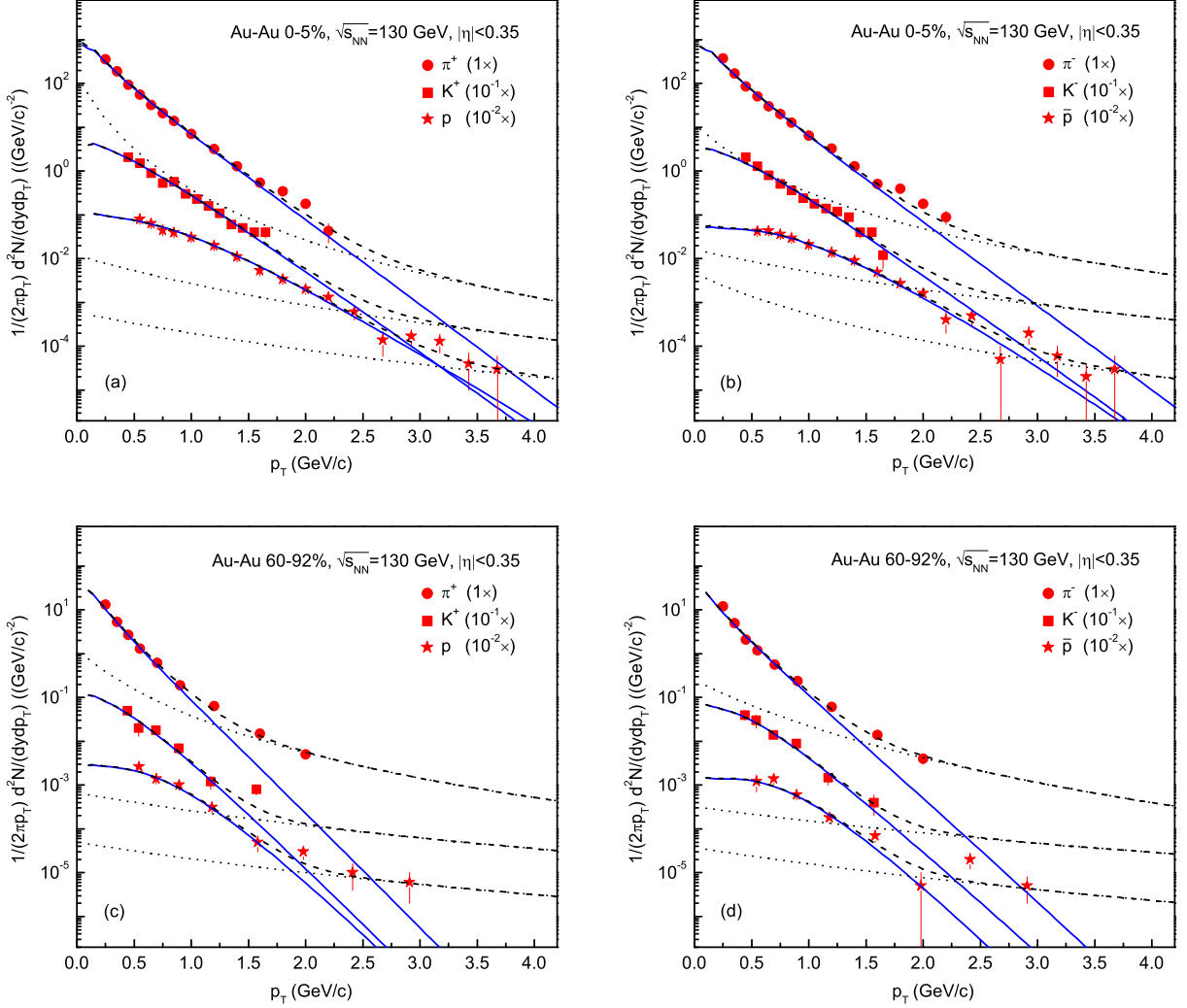


Fig. 3. Transverse momentum spectra of (a)-(c) π^+ , K^+ , and p , as well as (b)-(d) π^- , K^- , and \bar{p} produced in (a)-(b) 0-5% and (c)-(d) 60-92% Au-Au collisions at $\sqrt{s_{NN}} = 130$ GeV. The symbols represent the experimental data of the PHENIX Collaboration measured in $|\eta| < 0.35$ [23, 24] and scaled by different amounts shown in the panels. The solid, dotted, and dashed curves are our results calculated by using the improved Tsallis distribution [13, 14], the inverse power-law [30-32], and their superposition, respectively.

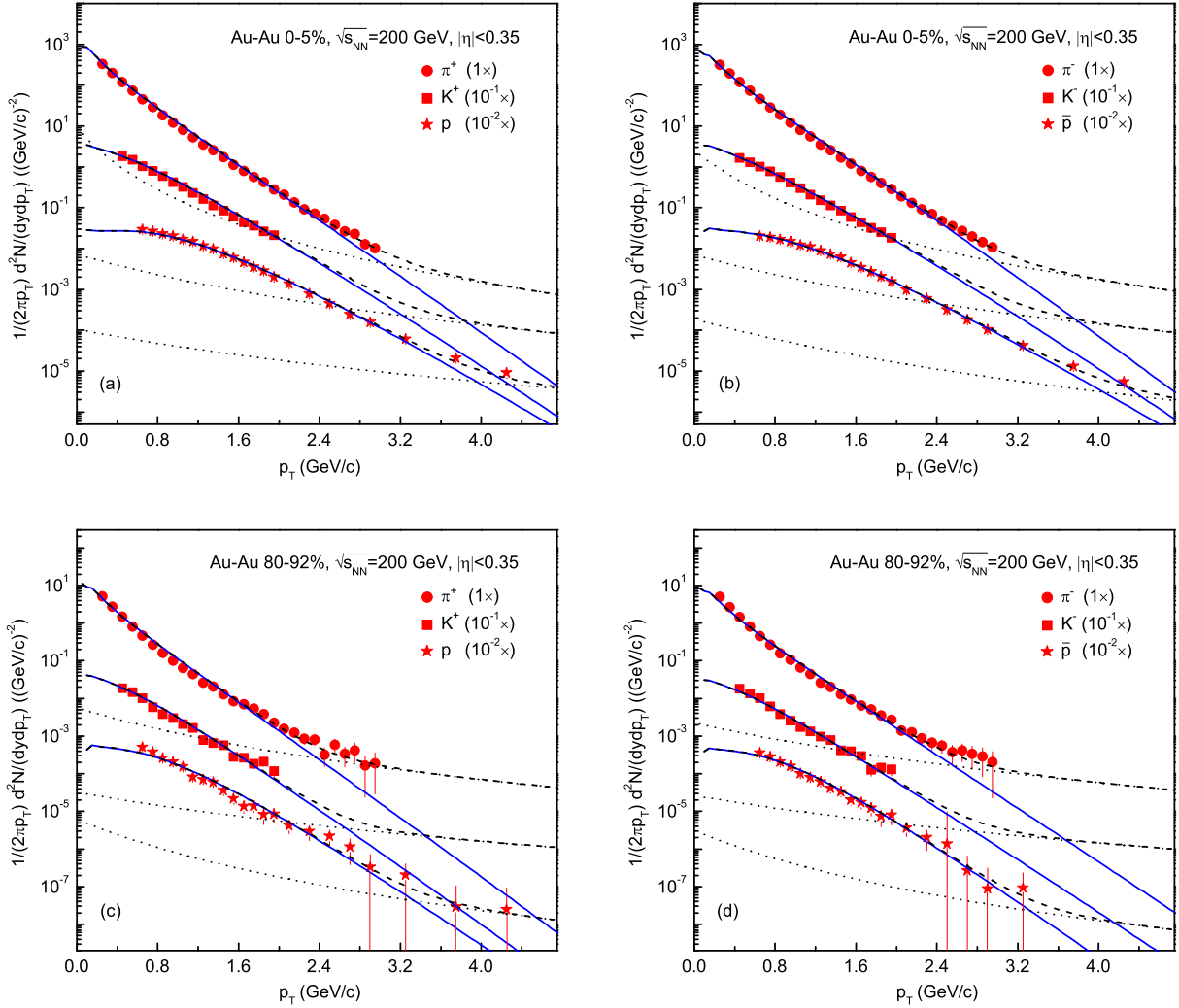


Fig. 4. Same as Figure 3, but showing the spectra for (a)-(c) π^+ , K^+ , and p , as well as (b)-(d) π^- , K^- , and \bar{p} produced in (a)-(b) 0-5% and (c)-(d) 80-92% Au-Au collisions at $\sqrt{s_{NN}} = 200$ GeV. The experimental data of the PHENIX Collaboration are taken from refs. [18, 25-28].

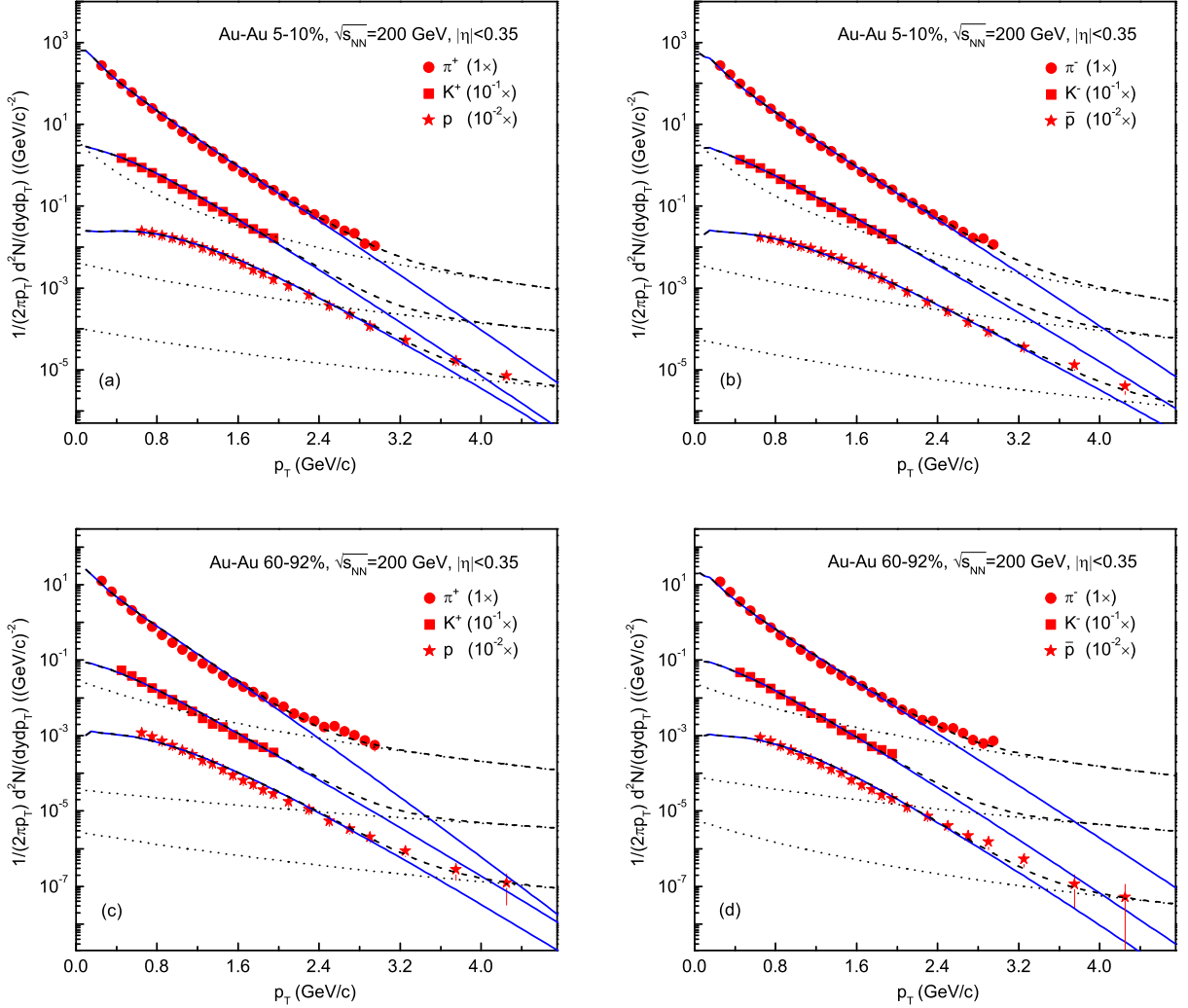


Fig. 5. Same as Figure 3, but showing the spectra for (a)-(c) π^+ , K^+ , and p , as well as (b)-(d) π^- , K^- , and \bar{p} produced in (a)-(b) 5–10% and (c)-(d) 60–92% Au-Au collisions at $\sqrt{s_{NN}} = 200$ GeV. The experimental data of the PHENIX Collaboration are taken from refs. [18, 25–28].

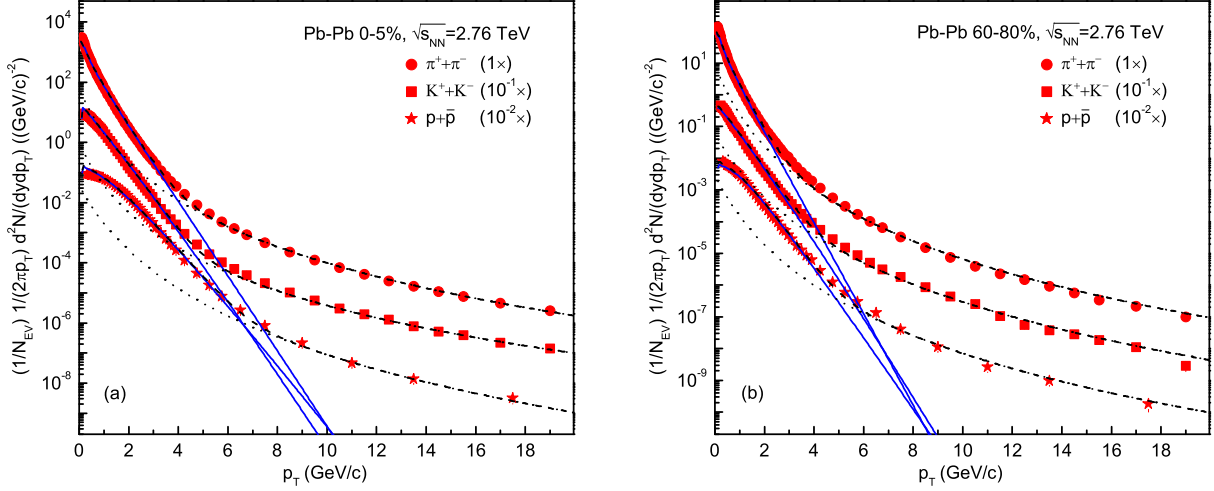


Fig. 6. Same as Figure 3, but showing the spectra for $\pi^+ + \pi^-$, $K^+ + K^-$, and $p + \bar{p}$ produced in (a) 0–5% and (b) 60–80% Pb-Pb collisions at $\sqrt{s_{NN}} = 2.76$ TeV. The experimental data of the ALICE Collaboration are taken from ref. [29] and measured in $|\eta| < 0.8$ for high p_T region and $|y| < 0.5$ for low p_T region.

Table 1. Values of free parameters (T_0 , q , and β_T), normalization constant (N_0), and χ^2/dof corresponding to the curves in Figures 1 and 2.

Figure	Centrality	Particle	T_0 (GeV)	q	β_T (c)	N_0	χ^2/dof
1(a)	0–5%	π^+	0.102 ± 0.004	1.011 ± 0.005	0.602 ± 0.023	108.589 ± 13.114	0.330
		K^+	0.109 ± 0.011	1.002 ± 0.001	0.574 ± 0.032	10.606 ± 1.683	0.974
		p	0.118 ± 0.009	1.003 ± 0.002	0.538 ± 0.023	10.525 ± 1.213	0.510
1(b)	0–5%	π^-	0.102 ± 0.004	1.011 ± 0.005	0.602 ± 0.023	108.589 ± 13.114	0.330
		K^-	0.102 ± 0.009	1.002 ± 0.001	0.558 ± 0.032	6.333 ± 1.017	0.469
		\bar{p}	0.115 ± 0.011	1.005 ± 0.003	0.531 ± 0.027	0.665 ± 0.053	0.448
1(c)	70–80%	π^+	0.091 ± 0.004	1.010 ± 0.008	0.604 ± 0.030	3.621 ± 0.628	0.248
		K^+	0.091 ± 0.009	1.002 ± 0.001	0.535 ± 0.030	0.224 ± 0.040	1.071
		p	0.091 ± 0.007	1.002 ± 0.001	0.499 ± 0.018	0.208 ± 0.029	1.057
2(a)	0–5%	π^+	0.088 ± 0.009	1.089 ± 0.055	0.605 ± 0.045	152.903 ± 11.752	1.907
		K^+	0.093 ± 0.012	1.049 ± 0.039	0.599 ± 0.028	14.564 ± 1.169	0.625
		p	0.110 ± 0.013	1.017 ± 0.015	0.588 ± 0.025	6.838 ± 0.388	4.341
2(b)	0–5%	π^-	0.091 ± 0.013	1.062 ± 0.032	0.604 ± 0.038	159.261 ± 16.224	3.201
		K^-	0.095 ± 0.012	1.051 ± 0.041	0.604 ± 0.028	12.253 ± 1.051	2.051
		\bar{p}	0.116 ± 0.011	1.002 ± 0.001	0.601 ± 0.014	3.113 ± 0.183	9.118
2(c)	70–80%	π^+	0.099 ± 0.009	1.005 ± 0.004	0.588 ± 0.038	5.061 ± 0.622	0.495
		K^+	0.104 ± 0.011	1.001 ± 0.0008	0.551 ± 0.028	0.350 ± 0.030	1.866
		p	0.104 ± 0.011	1.001 ± 0.0008	0.474 ± 0.025	0.209 ± 0.022	2.025
2(d)	70–80%	π^-	0.095 ± 0.009	1.015 ± 0.013	0.596 ± 0.038	5.233 ± 0.579	0.460
		K^-	0.095 ± 0.008	1.001 ± 0.0008	0.534 ± 0.029	0.325 ± 0.040	2.651
		\bar{p}	0.103 ± 0.011	1.001 ± 0.0008	0.449 ± 0.021	0.140 ± 0.015	4.580

Table 2. Values of free parameters (T_0 , q , β_T , k , p_0 , and n), normalization constant (N_0), and χ^2/dof corresponding to the curves in Figures 3–6.

Figure	Centrality	Particle	T_0 (GeV)	q	β_T (c)	k	p_0 (GeV/c)	n	N_0	χ^2/dof
3(a)	0–5%	π^+	0.109 ± 0.006	1.019 ± 0.015	0.558 ± 0.045	0.945 ± 0.052	0.425 ± 0.072	4.994 ± 0.912	195.464 ± 37.486	12.415
		K^+	0.115 ± 0.009	1.017 ± 0.015	0.537 ± 0.025	0.988 ± 0.041	2.805 ± 0.662	4.871 ± 0.072	17.615 ± 3.339	2.620
		p	0.131 ± 0.014	1.021 ± 0.020	0.531 ± 0.031	0.982 ± 0.015	3.988 ± 1.212	4.872 ± 0.895	7.311 ± 1.463	1.435
3(b)	0–5%	π^-	0.111 ± 0.005	1.010 ± 0.008	0.568 ± 0.025	0.976 ± 0.028	0.705 ± 0.082	4.105 ± 0.512	170.329 ± 26.755	18.306
		K^-	0.111 ± 0.009	1.012 ± 0.010	0.568 ± 0.029	0.965 ± 0.031	3.822 ± 0.454	4.964 ± 0.712	13.713 ± 1.436	2.435
		\bar{p}	0.111 ± 0.012	1.066 ± 0.052	0.568 ± 0.034	0.951 ± 0.041	1.407 ± 0.291	4.015 ± 0.812	4.786 ± 0.801	1.494
3(c)	60–92%	π^+	0.090 ± 0.009	1.022 ± 0.021	0.481 ± 0.045	0.917 ± 0.015	0.821 ± 0.135	4.408 ± 0.442	5.165 ± 0.603	18.640
		K^+	0.090 ± 0.013	1.015 ± 0.014	0.481 ± 0.051	0.901 ± 0.045	3.821 ± 0.632	4.104 ± 0.972	0.396 ± 0.053	8.166*
		p	0.090 ± 0.015	1.005 ± 0.004	0.481 ± 0.049	0.884 ± 0.021	4.449 ± 0.542	4.280 ± 0.545	0.196 ± 0.030	3.852
3(d)	60–92%	π^-	0.085 ± 0.009	1.021 ± 0.015	0.588 ± 0.035	0.952 ± 0.024	1.909 ± 0.045	5.697 ± 0.595	4.413 ± 0.539	40.442
		K^-	0.085 ± 0.009	1.014 ± 0.013	0.588 ± 0.044	0.908 ± 0.085	4.955 ± 0.958	4.068 ± 0.988	0.294 ± 0.060	2.931*
		\bar{p}	0.085 ± 0.009	1.007 ± 0.006	0.512 ± 0.049	0.869 ± 0.071	5.368 ± 0.682	4.986 ± 0.512	0.115 ± 0.019	9.566
4(a)	0–5%	π^+	0.109 ± 0.006	1.023 ± 0.016	0.634 ± 0.019	0.991 ± 0.008	0.709 ± 0.165	4.597 ± 0.645	224.148 ± 44.212	2.205
		K^+	0.113 ± 0.011	1.052 ± 0.037	0.634 ± 0.029	0.992 ± 0.007	2.594 ± 0.323	4.291 ± 0.935	16.743 ± 2.746	0.916
		p	0.121 ± 0.009	1.097 ± 0.055	0.634 ± 0.021	0.991 ± 0.007	3.697 ± 0.442	4.036 ± 0.834	3.191 ± 0.477	0.940
4(b)	0–5%	π^-	0.111 ± 0.006	1.062 ± 0.025	0.590 ± 0.032	0.994 ± 0.005	0.956 ± 0.218	4.436 ± 0.585	180.622 ± 38.234	1.529
		K^-	0.121 ± 0.011	1.067 ± 0.049	0.590 ± 0.031	0.991 ± 0.004	2.667 ± 0.331	4.286 ± 0.635	15.977 ± 4.268	1.087
		\bar{p}	0.133 ± 0.009	1.095 ± 0.065	0.590 ± 0.028	0.992 ± 0.007	3.132 ± 0.921	4.969 ± 0.812	2.777 ± 0.564	0.971
4(c)	80–92%	π^+	0.106 ± 0.009	1.028 ± 0.017	0.572 ± 0.026	0.994 ± 0.005	2.321 ± 0.461	4.382 ± 1.454	2.731 ± 0.449	3.616
		K^+	0.106 ± 0.008	1.028 ± 0.021	0.572 ± 0.055	0.991 ± 0.008	3.802 ± 0.395	4.161 ± 1.115	0.175 ± 0.032	1.847
		p	0.119 ± 0.009	1.013 ± 0.010	0.528 ± 0.035	0.992 ± 0.005	1.914 ± 0.258	4.945 ± 0.612	0.041 ± 0.003	1.551
4(d)	80–92%	π^-	0.115 ± 0.007	1.015 ± 0.012	0.587 ± 0.039	0.995 ± 0.004	3.419 ± 0.423	4.706 ± 0.612	2.161 ± 0.323	0.319
		K^-	0.115 ± 0.009	1.013 ± 0.011	0.587 ± 0.039	0.990 ± 0.006	3.922 ± 0.458	4.135 ± 0.995	0.137 ± 0.022	3.075
		\bar{p}	0.116 ± 0.009	1.005 ± 0.004	0.529 ± 0.038	0.995 ± 0.004	1.859 ± 0.423	4.796 ± 0.825	0.035 ± 0.005	0.523
5(a)	5–10%	π^+	0.111 ± 0.005	1.025 ± 0.015	0.635 ± 0.023	0.992 ± 0.006	0.742 ± 0.085	4.206 ± 0.681	168.336 ± 20.667	1.714
		K^+	0.111 ± 0.009	1.031 ± 0.025	0.635 ± 0.026	0.991 ± 0.008	3.191 ± 0.295	4.219 ± 0.045	13.864 ± 2.680	0.795
		p	0.118 ± 0.009	1.089 ± 0.055	0.635 ± 0.019	0.990 ± 0.005	4.271 ± 0.318	4.465 ± 0.052	2.872 ± 0.587	0.411
5(b)	5–10%	π^-	0.121 ± 0.007	1.026 ± 0.018	0.599 ± 0.029	0.992 ± 0.006	0.912 ± 0.182	4.973 ± 1.112	141.910 ± 31.630	1.155
		K^-	0.128 ± 0.013	1.039 ± 0.026	0.599 ± 0.039	0.993 ± 0.006	3.146 ± 0.235	4.546 ± 1.485	12.905 ± 1.965	1.051
		\bar{p}	0.139 ± 0.009	1.019 ± 0.015	0.599 ± 0.019	0.995 ± 0.004	3.695 ± 0.544	4.605 ± 0.385	2.336 ± 0.452	1.114
5(c)	60–92%	π^+	0.098 ± 0.007	1.068 ± 0.025	0.608 ± 0.019	0.991 ± 0.005	1.912 ± 0.852	4.425 ± 0.745	5.295 ± 1.115	3.382
		K^+	0.121 ± 0.011	1.015 ± 0.012	0.608 ± 0.036	0.989 ± 0.010	5.689 ± 0.995	3.879 ± 0.835	0.395 ± 0.207	2.223
		p	0.126 ± 0.009	1.032 ± 0.026	0.558 ± 0.019	0.992 ± 0.005	4.578 ± 0.985	4.887 ± 1.152	0.103 ± 0.011	1.990
5(d)	60–92%	π^-	0.114 ± 0.006	1.026 ± 0.012	0.599 ± 0.035	0.992 ± 0.007	2.188 ± 0.242	4.857 ± 1.445	5.244 ± 0.970	2.671
		K^-	0.114 ± 0.006	1.030 ± 0.018	0.575 ± 0.038	0.990 ± 0.003	4.393 ± 0.812	4.506 ± 0.758	0.403 ± 0.055	2.913
		\bar{p}	0.114 ± 0.007	1.026 ± 0.021	0.556 ± 0.025	0.994 ± 0.005	2.187 ± 0.545	4.475 ± 0.915	0.088 ± 0.010	1.128
6(a)	0–5%	π^\pm	0.161 ± 0.009	1.009 ± 0.008	0.612 ± 0.034	0.976 ± 0.007	1.440 ± 0.144	6.438 ± 0.196	667.706 ± 118.159	3.901
		K^\pm	0.162 ± 0.009	1.049 ± 0.041	0.612 ± 0.033	0.976 ± 0.007	1.272 ± 0.129	5.742 ± 0.205	72.995 ± 11.077	2.196
		$p + \bar{p}$	0.192 ± 0.012	1.075 ± 0.055	0.612 ± 0.023	0.961 ± 0.011	2.073 ± 0.169	7.349 ± 0.251	14.629 ± 2.695	6.755
6(b)	60–80%	π^\pm	0.135 ± 0.011	1.011 ± 0.010	0.630 ± 0.033	0.914 ± 0.021	1.426 ± 0.094	6.779 ± 0.146	25.246 ± 4.326	6.775
		K^\pm	0.158 ± 0.014	1.048 ± 0.041	0.608 ± 0.035	0.921 ± 0.019	2.144 ± 0.172	7.045 ± 0.198	2.124 ± 0.441	4.190
		$p + \bar{p}$	0.176 ± 0.015	1.017 ± 0.015	0.598 ± 0.039	0.922 ± 0.018	1.899 ± 0.045	7.059 ± 0.147	0.611 ± 0.105	2.926

* This is χ^2 only due to the dof being less than 1.

Table 3. Values of parameters (a , b , and c) and χ^2/dof corresponding to the curves in Figure 7. The function for the curves in Figure 7 is $T_0 = a(\sqrt{s_{NN}})^b + c$.

Figure	Main particle	a	b	c	χ^2/dof
7(a)	π^+	$(1.442 \pm 0.115) \times 10^{-3}$	0.498 ± 0.021	0.086 ± 0.004	3.479
	K^+	$(1.462 \pm 0.151) \times 10^{-3}$	0.487 ± 0.022	0.094 ± 0.003	0.740
	p	$(1.432 \pm 0.235) \times 10^{-3}$	0.511 ± 0.019	0.107 ± 0.005	1.078
7(b)	π^-	$(1.462 \pm 0.252) \times 10^{-3}$	0.481 ± 0.029	0.094 ± 0.009	1.048
	K^-	$(1.462 \pm 0.232) \times 10^{-3}$	0.478 ± 0.025	0.097 ± 0.007	0.767
	\bar{p}	$(1.462 \pm 0.199) \times 10^{-3}$	0.513 ± 0.020	0.107 ± 0.005	0.941
7(c)	π^+	$(1.462 \pm 0.225) \times 10^{-3}$	0.446 ± 0.021	0.085 ± 0.005	0.551
	K^+	$(1.462 \pm 0.235) \times 10^{-3}$	0.492 ± 0.015	0.086 ± 0.005	1.051
	p	$(1.462 \pm 0.193) \times 10^{-3}$	0.518 ± 0.015	0.087 ± 0.006	1.822
7(d)	π^-	$(1.462 \pm 0.213) \times 10^{-3}$	0.453 ± 0.022	0.082 ± 0.004	7.138
	K^-	$(1.462 \pm 0.202) \times 10^{-3}$	0.498 ± 0.013	0.083 ± 0.004	3.669
	\bar{p}	$(1.462 \pm 0.165) \times 10^{-3}$	0.522 ± 0.015	0.084 ± 0.004	2.973

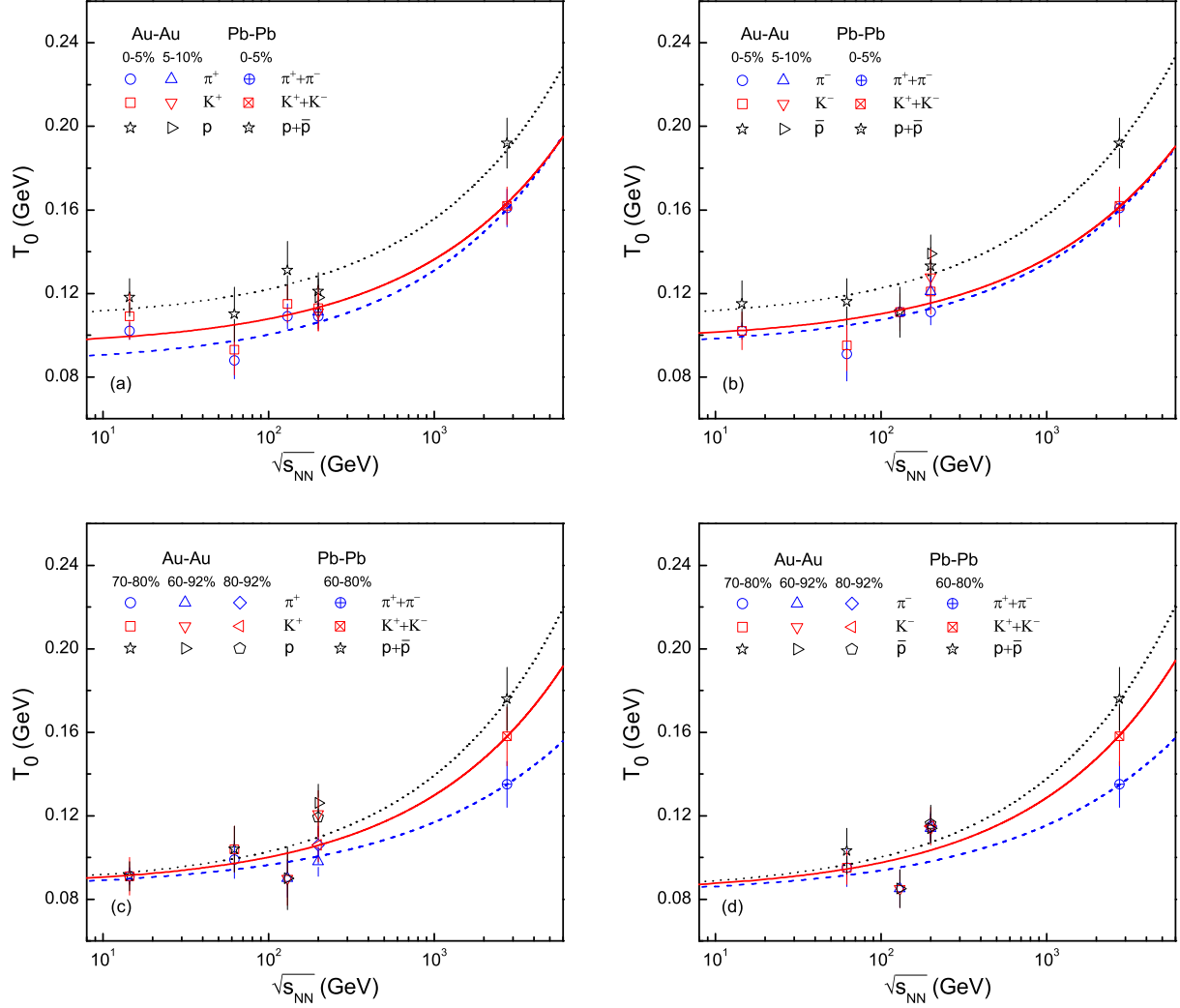


Fig. 7. Dependences of T_0 on $\sqrt{s_{NN}}$ for (a)-(c) positively and (b)-(d) negatively charged particles in (a)-(b) central and (c)-(d) peripheral Au-Au collisions at different energies, as well as for charged particles in (a)-(b) central and (c)-(d) peripheral Pb-Pb collisions at 2.76 TeV. The symbols represent T_0 extracted from different spectra for different particles in different collisions listed in Tables 1 and 2 and shown in the panels. The dashed, solid, and dotted curves are our results fitted by using the method of least squares for charged pions, kaons, and protons (antiprotons), respectively.

in central collisions. In most cases, the differences in q for different particles are not obvious.

The parameter β_T increases slightly with the increase of $\sqrt{s_{NN}}$. Moreover, the present work also extracted a slightly larger β_T in central collisions than in peripheral collisions, which is partly inconsistent with the blast-wave model which gives non-zero flow velocity in central collisions and zero flow velocity in peripheral collisions [11, 12, 20, 22, 33]. The present work confirms our recent work [17] which used the alternative method and obtained a slightly larger β_T in central collisions than in peripheral collisions, though the values obtained in the present work are slightly larger than those in our recent work. In our opinion, the flow is produced in the inner core of the interacting system. Even for peripheral or proton-proton collisions, there is non-zero flow velocity. From Figure 9, one can also see the mass-dependence of β_T in most cases. A heavy particle corresponds to a small β_T due to its large inertia. The differences in β_T for different particles decrease with the increase of $\sqrt{s_{NN}}$, where β_T is large at high $\sqrt{s_{NN}}$. This reflects the fact that the mass effect can be neglected in a strong flow field.

With increasing $\sqrt{s_{NN}}$, p_0 decreases in some cases and n increases obviously, their function $f_H(p_T)$ describes a wider p_T range, though their tendencies seem to be opposite to each other. According to the relation $n = 1/(q - 1)$ [14], we know that the hard scattering process corresponds to a larger q which makes the collisions be farther away from the equilibrium state when comparing with the soft excitation process. According to the relation $p_0 = T_0/(q - 1) = T_0 n$ [14], we know that the hard process corresponds to a higher T_0 , which results in more violent collisions than is the soft process. This observation is a natural result. The differences in p_0 and in n for central and peripheral collisions, as well as for different particle productions, are not obvious. This reflects the fact that, in the hard process, the participant valence quarks collide deeply at the initial state where the spectator nucleons have no effect.

The relative contribution (k) of the soft excitation process decreases slightly and the relative contribution ($1 - k$) of the hard scattering process increases slightly with the increase of $\sqrt{s_{NN}}$. This is consistent with the theoretical expectation [34, 35], and inconsistent with the extraction based on the numbers of participating nucleons and binary nucleon-nucleon collisions [36, 37]. In our opinion, at higher energy, both the participant valence quarks have more probability to approach each other and to perform interactions. Then, the hard process has more contribution to the p_T spectrum. However, the participant gluons and/or sea quarks have less time to perform interactions due to the higher pass speed at higher energy, which means that the soft process contributes less to the p_T spectrum. The differences

in k for central and peripheral collisions, as well as for different particle productions, are not obvious. This also reflects the fact that in the hard process the participant valence quarks collide deeply at the initial state where the spectator nucleons have no effect.

Generally, the yields of the soft process and the soft plus hard processes shown in Figures 13 and 14 increase with the increase of $\sqrt{s_{NN}}$ except for protons that saturate due to the limited proton numbers in the participant nuclei. Obviously, the yield for π^\pm is greater than that for K^\pm , and much greater than that for \bar{p} . The yield for central collisions is greater than that for peripheral collisions. The yield for positive mesons is slightly greater than that for negative mesons. These tendencies of the yields are natural results due to the experimental data analyzed in the present work.

From the above discussions, in particular from Figures 7–14 and Tables 1–4 one can see that, not only for the dependence on $\sqrt{s_{NN}}$ but also for the dependence on centrality, all the free parameters in the improved Tsallis distribution and in the inverse power-law seem to be independent of isospin. This means that electromagnetic interactions play a minor role in both the soft and hard processes.

We would like to point out that, as can be seen from Tables 1 and 2, the model fitting is not very good in a few cases, because the values of χ^2/dof are very large for these cases. That does not mean that the model cannot describe the particle distributions in heavy ion collisions. In fact, in most cases, we have obtained appropriate values of χ^2/dof which imply that the model works well. The very large values of χ^2/dof are obtained due to abnormally small errors. In the case of using a relative error being 5%, the values of χ^2/dof are appropriate. From Tables 3 and 4 one can see that the values of χ^2/dof are very large in many cases. That means that the relations $Y = a + b \ln(\sqrt{s_{NN}})$ and $Y = \exp[a + b \ln(\sqrt{s_{NN}})]$ assumed by us do not work well.

In the above discussions, we have used six free parameters, the kinetic freeze-out temperature T_0 , the entropy index q , the radial velocity flow β_T , the fraction k of soft component, p_0 , and n . The meanings of the first four parameters are clear. The meanings of the last two parameters can result from the relations $p_0 = T_0/(q - 1)$ and $n = 1/(q - 1)$ [14] which show that p_0 has a similar meaning to T_0 and n has an opposite meaning in comparison with q . In many cases, the mass-dependent tendencies of these parameters are not obvious because they are just from the model fittings. In addition, to obtain the mass-dependent tendencies of these parameters, we need more types of particles.

The present work shows that the interacting systems at the LHC have a higher excitation and larger expansion than those at the RHIC due to a greater en-

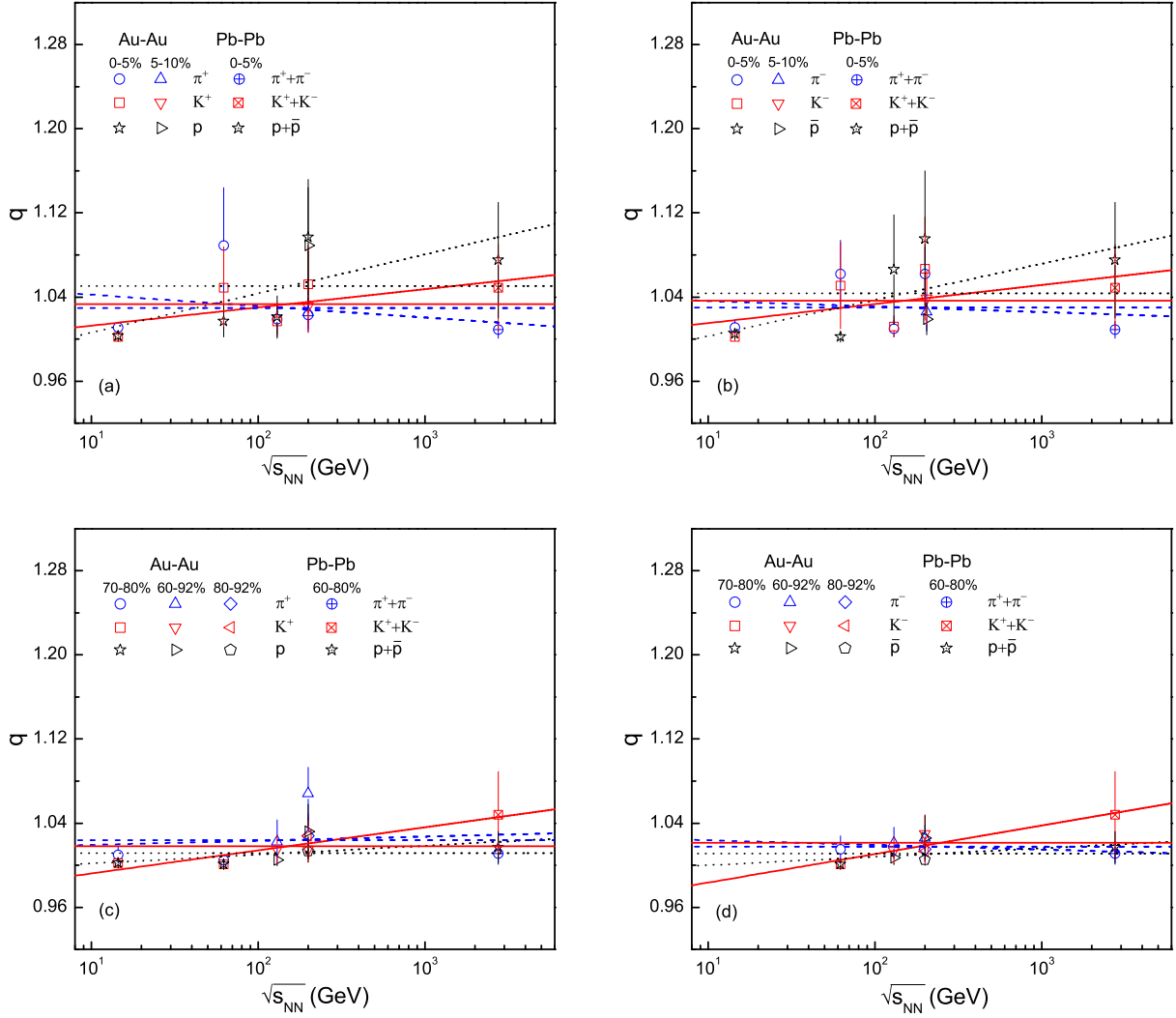


Fig. 8. Same as Figure 7, but showing the dependences of q on $\sqrt{s_{NN}}$. The horizontal dashed, solid, and dotted lines represent the mean values of q over different energies for charged pions, kaons, and protons (antiprotons), respectively.

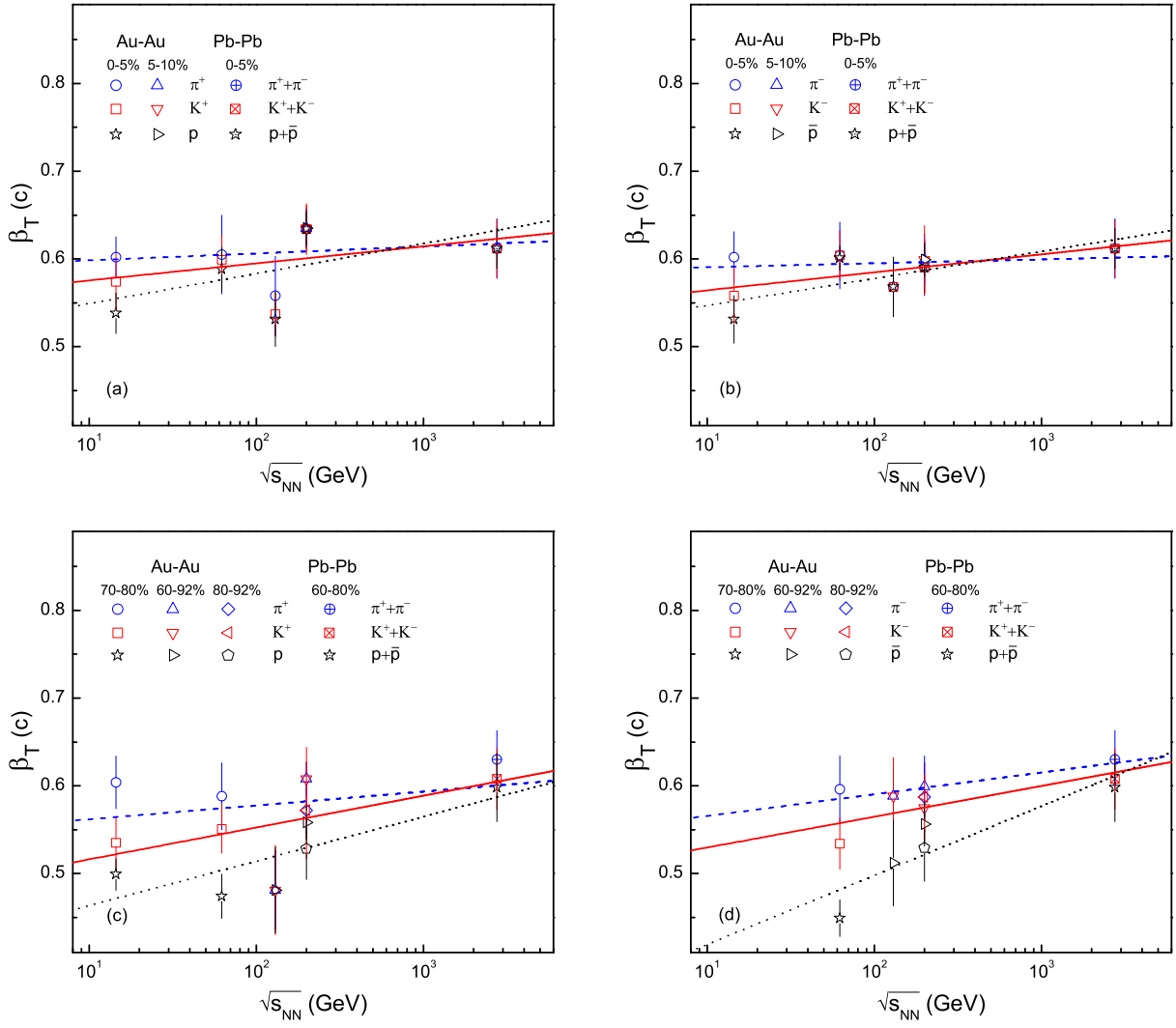


Fig. 9. Same as Figure 7, but showing the dependences of β_T on $\sqrt{s_{NN}}$.

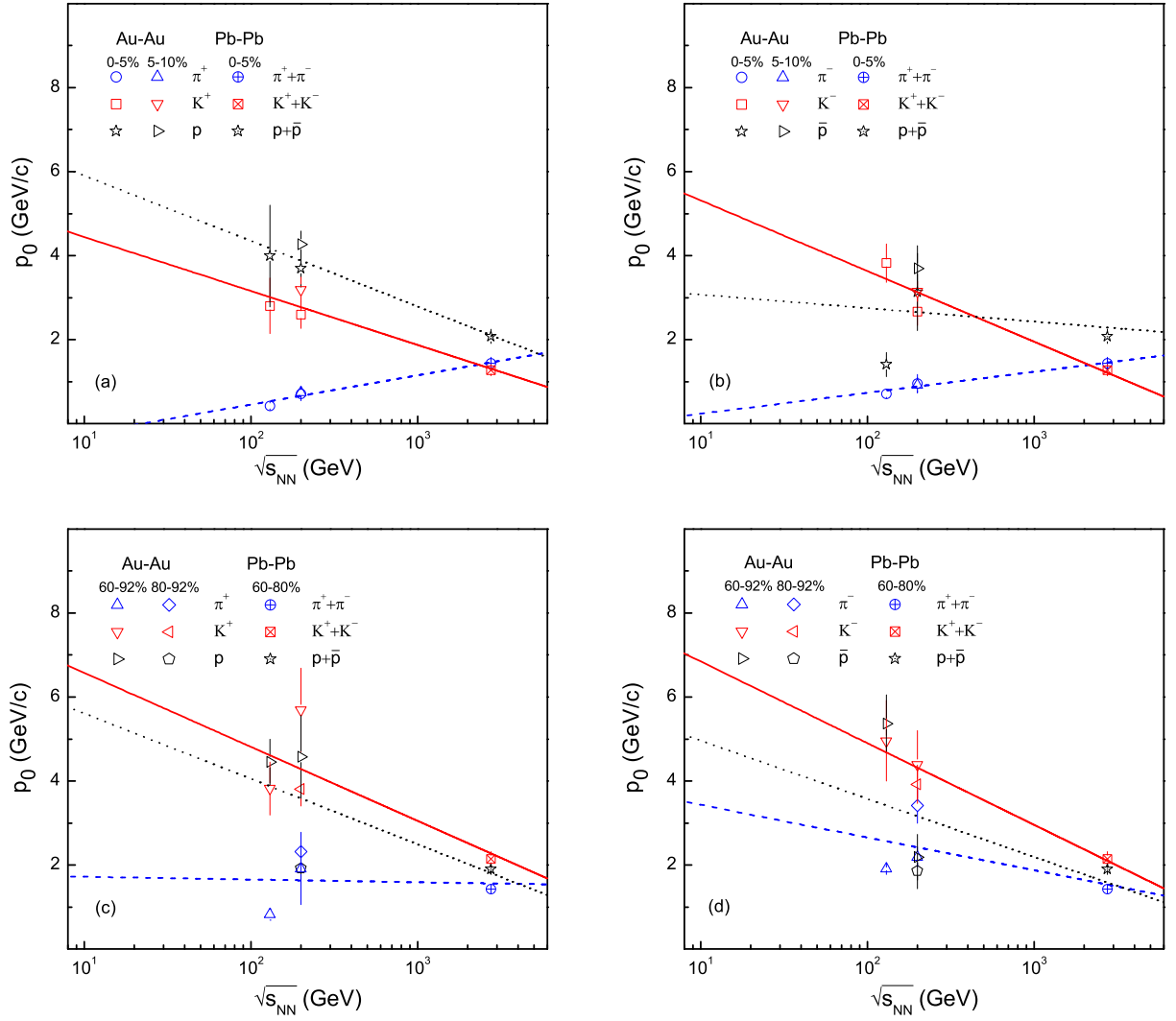


Fig. 10. Same as Figure 7, but showing the dependences of p_0 on $\sqrt{s_{NN}}$.

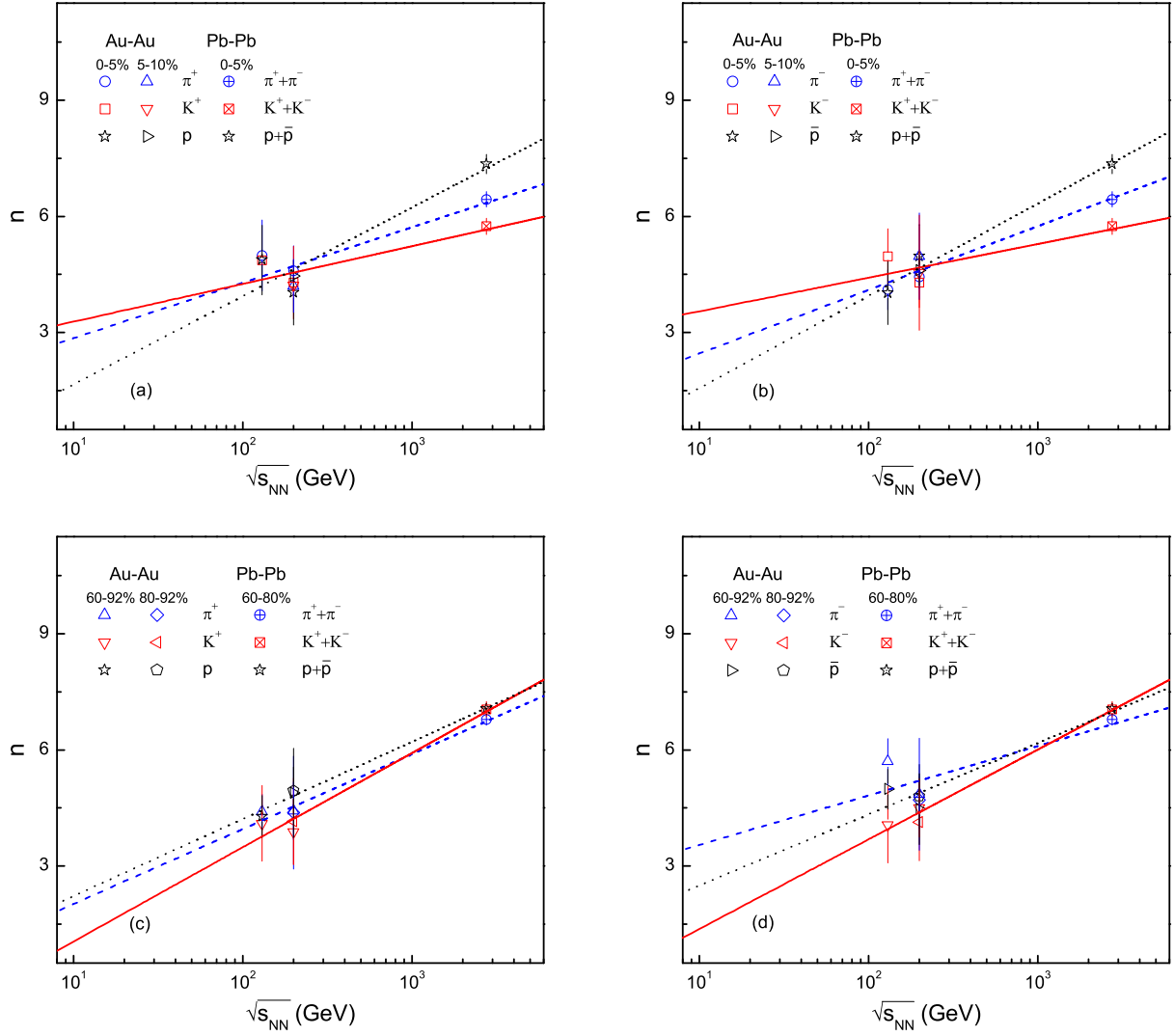


Fig. 11. Same as Figure 7, but showing the dependences of n on $\sqrt{s_{NN}}$.

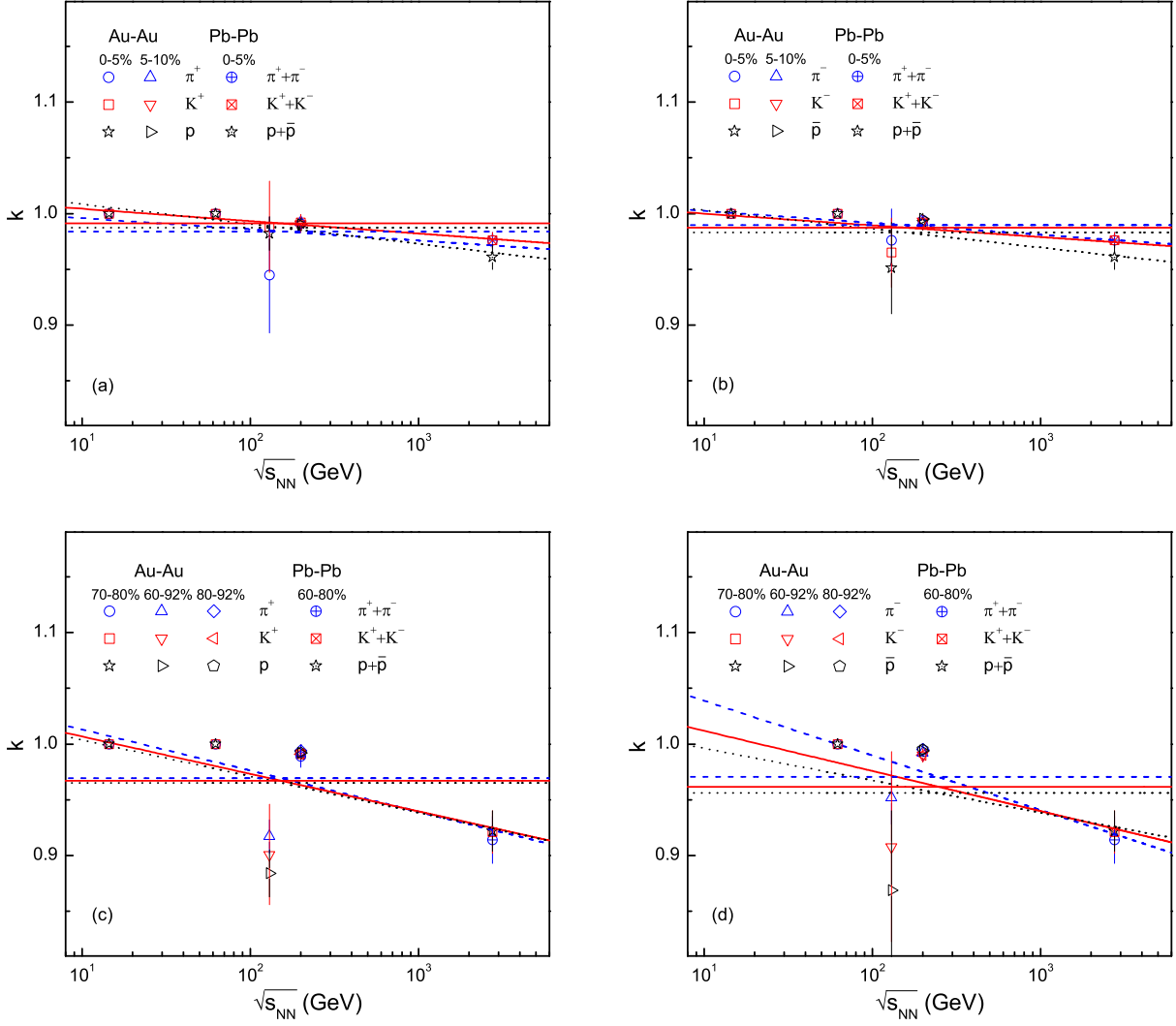


Fig. 12. Same as Figure 7, but showing the dependences of k on $\sqrt{s_{NN}}$. The horizontal dashed, solid, and dotted lines represent the mean values of k over different energies for charged pions, kaons, and protons (antiprotons), respectively.

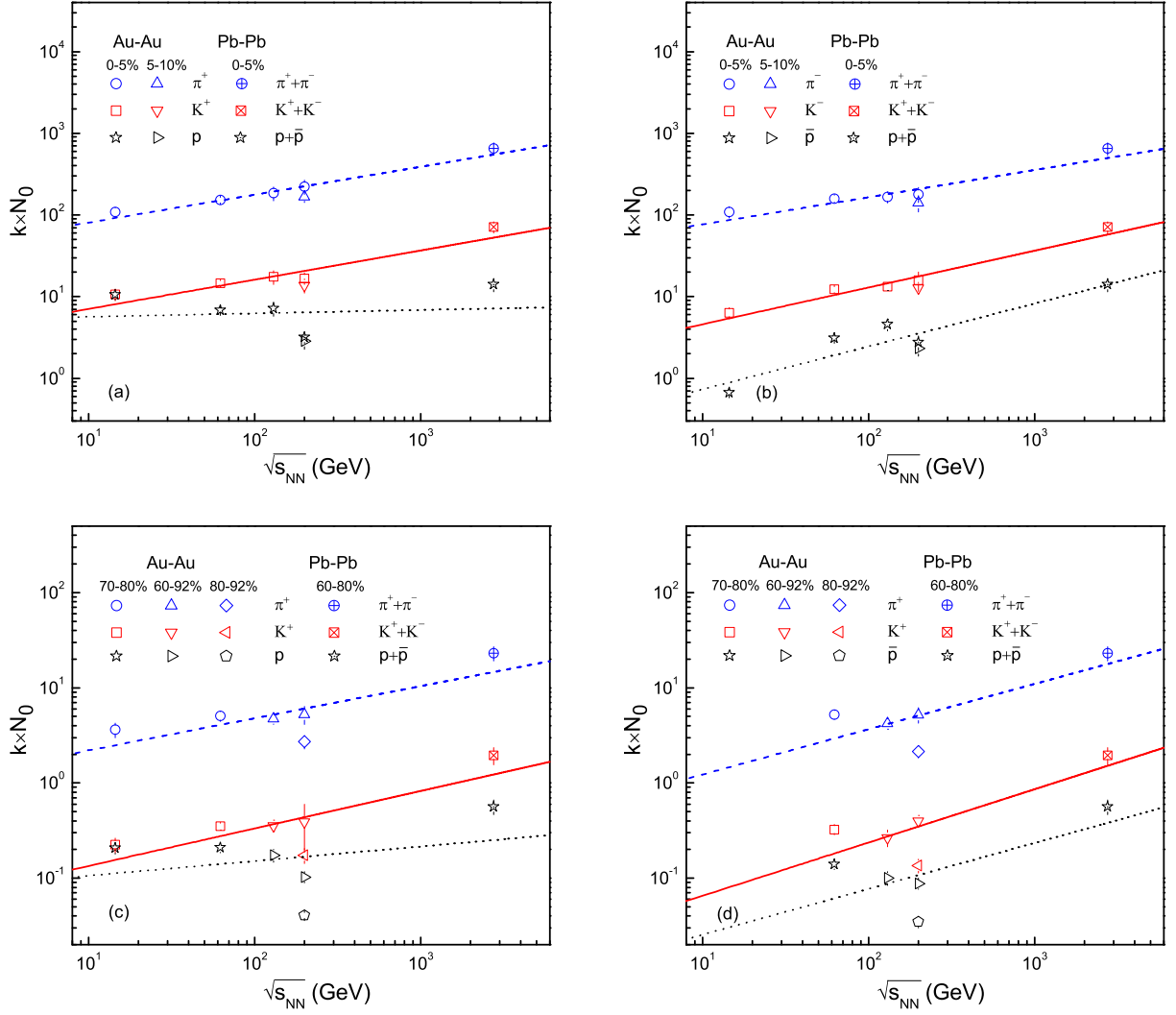


Fig. 13. Same as Figure 7, but showing the dependences of kN_0 on $\sqrt{s_{NN}}$, where the product kN_0 represents the yield of soft excitation process.

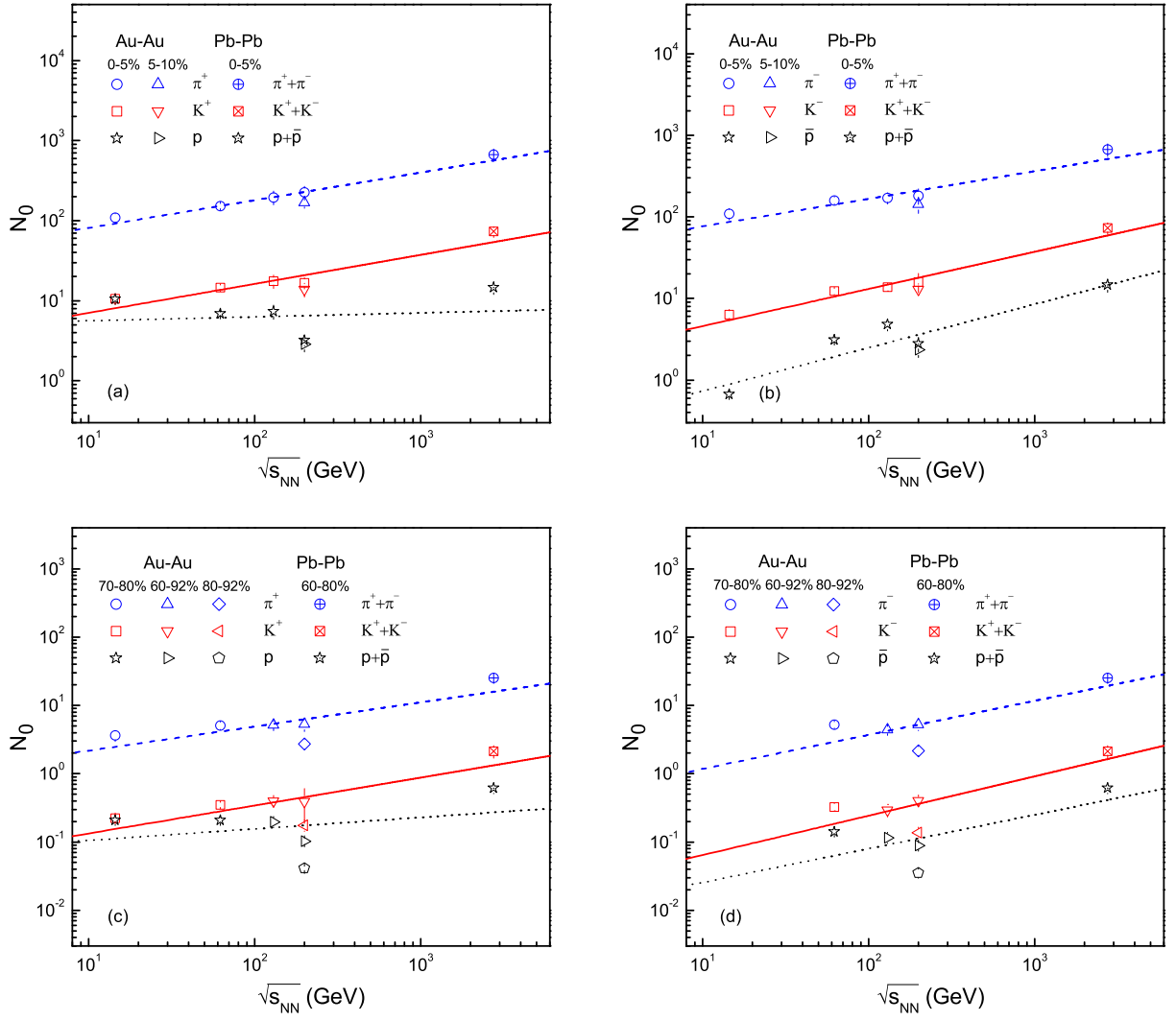


Fig. 14. Same as Figure 7, but showing the dependences of N_0 on $\sqrt{s_{NN}}$.

Table 4. Values of parameters (a and b) and χ^2/dof corresponding to the curves in Figures 8–14. The function for the curves in Figures 8–12 is $Y = a + b \ln(\sqrt{s_{NN}})$, where $Y = q, \beta_T, p_0, n,$ or k . The function for the curves in Figures 13 and 14 is $Y = \exp[a + b \ln(\sqrt{s_{NN}})]$, where $Y = kN_0$ or N_0 .

Figure	Y	Main particle	a	b	χ^2/dof
8(a)	q	π^+	1.053 ± 0.039	-0.005 ± 0.007	9.284
		K^+	0.995 ± 0.022	0.008 ± 0.004	46.487
		p	0.969 ± 0.042	0.016 ± 0.008	6.489
8(b)		π^-	1.041 ± 0.035	-0.002 ± 0.007	6.117
		K^-	0.997 ± 0.028	0.008 ± 0.005	66.313
		\bar{p}	0.968 ± 0.042	0.015 ± 0.008	200.674
8(c)		π^+	1.015 ± 0.031	0.002 ± 0.006	6.725
		K^+	0.970 ± 0.009	0.010 ± 0.002	38.944
		p	0.993 ± 0.014	0.004 ± 0.003	22.203
8(d)		π^-	1.028 ± 0.010	-0.002 ± 0.002	0.243
		K^-	0.956 ± 0.013	0.012 ± 0.002	8.679
		\bar{p}	0.992 ± 0.017	0.004 ± 0.003	15.919
9(a)	β_T	π^+	0.591 ± 0.038	0.003 ± 0.007	1.085
		K^+	0.556 ± 0.048	0.008 ± 0.009	2.261
		p	0.515 ± 0.052	0.015 ± 0.010	3.215
9(b)		π^-	0.586 ± 0.021	0.002 ± 0.004	0.390
		K^-	0.544 ± 0.020	0.009 ± 0.004	0.318
		\bar{p}	0.516 ± 0.026	0.013 ± 0.005	1.450
9(c)		π^+	0.546 ± 0.070	0.007 ± 0.013	2.362
		K^+	0.480 ± 0.055	0.016 ± 0.010	1.000
		p	0.413 ± 0.040	0.022 ± 0.008	1.623
9(d)		π^-	0.541 ± 0.016	0.011 ± 0.003	0.065
		K^-	0.495 ± 0.033	0.015 ± 0.006	0.328
		\bar{p}	0.340 ± 0.049	0.034 ± 0.009	1.496
10(a)	p_0	π^+	-0.941 ± 0.202	0.303 ± 0.034	1.594
		K^+	5.731 ± 0.714	-0.558 ± 0.119	1.245
		p	7.462 ± 0.669	-0.676 ± 0.112	0.874
10(b)		π^-	-0.266 ± 0.165	0.217 ± 0.028	0.616
		K^-	6.999 ± 0.854	-0.731 ± 0.143	1.437
		\bar{p}	3.392 ± 2.492	-0.139 ± 0.417	12.848
10(c)		π^+	1.784 ± 1.589	-0.028 ± 0.266	20.942
		K^+	8.341 ± 2.403	-0.766 ± 0.402	2.815
		p	7.168 ± 2.886	-0.677 ± 0.483	24.165
10(d)		π^-	4.211 ± 1.739	-0.338 ± 0.291	110.619
		K^-	8.794 ± 0.695	-0.845 ± 0.116	0.451
		\bar{p}	6.347 ± 3.638	-0.602 ± 0.609	35.699
11(a)	n	π^+	1.426 ± 1.084	0.621 ± 0.182	0.582
		K^+	2.307 ± 0.940	0.423 ± 0.157	51.514
		p	-0.620 ± 1.305	0.992 ± 0.219	6.059
11(b)		π^-	0.819 ± 0.640	0.713 ± 0.107	0.172
		K^-	2.677 ± 0.874	0.378 ± 0.146	0.458
		\bar{p}	-0.815 ± 0.530	1.035 ± 0.089	0.123
11(c)		π^+	0.091 ± 0.432	0.839 ± 0.072	0.188
		K^+	-1.375 ± 0.693	2.430 ± 0.267	0.185
		p	0.242 ± 0.315	0.864 ± 0.053	0.087
11(d)		π^-	2.273 ± 1.363	0.554 ± 0.228	1.451
		K^-	-0.941 ± 0.429	1.006 ± 0.072	0.056
		\bar{p}	0.660 ± 0.877	0.799 ± 0.147	0.598
12(a)	k	π^+	1.006 ± 0.027	-0.004 ± 0.005	12.283
		K^+	1.015 ± 0.004	-0.005 ± 0.001	6.715
		p	1.026 ± 0.008	-0.008 ± 0.002	4.428
12(b)		π^-	1.013 ± 0.010	-0.005 ± 0.002	2.861
		K^-	1.010 ± 0.016	-0.005 ± 0.003	5.422
		\bar{p}	1.020 ± 0.024	-0.007 ± 0.005	10.366
12(c)		π^+	1.050 ± 0.043	-0.016 ± 0.008	27.256
		K^+	1.040 ± 0.049	-0.015 ± 0.009	16.334
		p	1.036 ± 0.059	-0.014 ± 0.011	30.668
12(d)		π^-	1.088 ± 0.041	-0.021 ± 0.007	10.944
		K^-	1.048 ± 0.074	-0.016 ± 0.013	34.967
		\bar{p}	1.025 ± 0.109	-0.013 ± 0.019	54.566
13(a)	kN_0	π^+	3.603 ± 0.235	0.342 ± 0.045	2.604
		K^+	1.132 ± 0.378	0.358 ± 0.072	3.700
		p	1.638 ± 0.867	0.042 ± 0.164	27.912
13(b)		π^-	3.569 ± 0.344	0.334 ± 0.065	2.535
		K^-	0.484 ± 0.286	0.451 ± 0.054	3.152
		\bar{p}	-1.520 ± 0.542	0.525 ± 0.103	18.802
13(c)		π^+	0.010 ± 0.630	0.338 ± 0.119	16.824
		K^+	-2.915 ± 0.690	0.394 ± 0.131	20.334
		p	-2.596 ± 1.136	0.153 ± 0.215	473.659
13(d)		π^-	-0.892 ± 1.057	0.476 ± 0.187	34.078
		K^-	-4.022 ± 1.130	0.560 ± 0.200	36.881
		\bar{p}	-4.783 ± 1.450	0.482 ± 0.257	83.614
14(a)	N_0	π^+	3.597 ± 0.235	0.346 ± 0.045	2.693
		K^+	1.117 ± 0.379	0.363 ± 0.072	3.717
		p	1.612 ± 0.873	0.049 ± 0.166	26.466
14(b)		π^-	3.556 ± 0.345	0.338 ± 0.065	2.522
		K^-	0.474 ± 0.284	0.455 ± 0.054	3.052
		\bar{p}	-1.540 ± 0.556	0.533 ± 0.106	18.784
14(c)		π^+	-0.042 ± 0.647	0.354 ± 0.123	18.303
		K^+	-2.957 ± 0.705	0.409 ± 0.134	21.883
		p	-2.633 ± 1.158	0.168 ± 0.220	517.425
14(d)		π^-	-0.984 ± 1.076	0.498 ± 0.190	36.226
		K^-	-4.071 ± 1.141	0.576 ± 0.202	39.466
		\bar{p}	-4.807 ± 1.484	0.495 ± 0.263	93.005

ergy depositions at the LHC. The central collisions have a higher excitation and larger expansion than the peripheral collisions due to greater energy depositions in the central collisions. Both the central and peripheral collisions are approximately in the equilibrium states, though the peripheral collisions are closer to the equilibrium state. Comparing with that at the RHIC, the transverse momentum spectrum at the LHC has a lower fraction of soft component, because the participant gluons and/or sea quarks have less time to perform interactions in the case of the heavy ions having higher pass speed at the LHC.

It should be noted that the same information can be obtained from other methods, and the values for the same quantities from different methods are different. In other words, the results are model dependent. In particular, for the kinetic freeze-out temperature or the radial flow velocity, different methods can be regarded as different ‘thermometers’ or ‘speedometers’. To make a comparison for the results obtained from different methods, we need to structure a standard method which can be used to make comparison with others. Or, we can use the alternative method in which T_0 is regarded as the intercept in the linear relation between T and m_0 [11, 18–20], and β_T is regarded as the slope in the linear relation between $\langle p_T \rangle$ and $\langle m \rangle$ [15–17].

4 Conclusions

We summarize here our main observations and conclusions.

(a) The p_T spectra of π^\pm , K^\pm , p , and \bar{p} produced in Au-Au and Pb-Pb collisions over an energy $\sqrt{s_{NN}}$ range from 14.5 GeV to 2.76 TeV have been analyzed. For the spectra with a narrow p_T range, the improved Tsallis distribution which describes the soft process is used. For the spectra with a wide p_T range, the superposition of the improved Tsallis distribution and the inverse power-law which describes the hard process is used. The modelling results are in approximate agreement with the experimental data measured by the STAR, PHENIX, and ALICE Collaborations. Some parameters are extracted due to the fittings.

(b) Both the extracted T_0 and β_T increase with the increase of $\sqrt{s_{NN}}$, which indicates a higher excitation and larger expansion of the interesting system at the LHC. Both the values of T_0 and β_T in central collisions are slightly larger than those in peripheral collisions. The slight differences in T_0 for different particles are observed in some cases. This confirms the mass-dependent differential kinetic freeze-out scenario. An evidence of mass-dependent β_T is observed in most cases. A heavy particle corresponds to a small β_T due to its large inertia. The differences in β_T for different particles decrease with the increase of $\sqrt{s_{NN}}$. The mass-dependent effect

of β_T can be neglected in a strong flow field at the LHC.

(c) The parameter q increases slightly with the increase of $\sqrt{s_{NN}}$, but the dependence of q on $\sqrt{s_{NN}}$ is not obvious. The parameters q in central and peripheral collisions are very small, which means that the two types of collisions are in the nearly equilibrium state respectively, though a slight larger q seems to be observed in central collisions. In most cases, the differences in q for different particles are not obvious. The relative contribution k of the soft process decreases slightly with the increase of $\sqrt{s_{NN}}$. At the LHC, the participant gluons and/or sea quarks have less time to perform interactions due to higher pass speed, which means that the soft process contributes less to the p_T spectrum. The differences in k for central and peripheral collisions, as well as for different particle productions, are not obvious.

(d) With increasing $\sqrt{s_{NN}}$, p_0 decreases in some cases and n increases obviously, their function $f_H(p_T)$ describes a wider p_T range. The differences in p_0 and in n for central and peripheral collisions, as well as for different particle productions, are not obvious. This reflects the fact that, in the hard process, the participant valence quarks collide deeply at the initial state where the spectator nucleons have no effect. The relative contribution $1 - k$ of the hard process increases slightly with the increase of $\sqrt{s_{NN}}$. At higher energy, both the participant valence quarks have more probability to approach each other and to perform interactions. Then, the hard process has more contribution to the p_T spectrum at the LHC. Our conclusion is in agreement with the theoretical prediction based on QCD.

(e) The yields of the soft process and the soft plus hard processes increase with the increase of $\sqrt{s_{NN}}$ except for protons that saturate due to the limited proton numbers in the participant nuclei. The yield for π^\pm is greater than that for K^\pm , and much greater than that for \bar{p} . The yield for central collisions is greater than that for peripheral collisions. The yield for positive mesons is slightly greater than that for negative mesons. These tendencies of the yields appear due to the experimental data themselves. In fact, the yields are the normalization constants. Not only for the dependence on $\sqrt{s_{NN}}$ but also for the dependence on centrality, all the free parameters in the improved Tsallis distribution and in the inverse power-law seem to be independent of isospin. This means that electromagnetic interactions play a minor role in both the soft and hard processes.

Conflict of Interests

The authors declare that there is no conflict of interests regarding the publication of this paper.

Acknowledgments

This work was supported by the National Natural Science Foundation of China under Grant No.

References

- [1] J.L. Synge, *The Relativistic Gas* (North-Holland, Amsterdam, The Netherlands, 1957).
- [2] P.Z. Ning, L. Li, D.F. Min, *Foundation of Nuclear Physics: Nucleons and Nuclei* (Higher Education Press, Beijing, China, 2003).
- [3] C.D. Dermer, *Astrophys. J.* **280**, 328 (1984).
- [4] J. Cleymans, D. Worku, *Eur. Phys. J. A* **48**, 160 (2012).
- [5] C. Tsallis, *J. Stat. Phys.* **52**, 479 (1988).
- [6] T.S. Biró, G. Purcsel, K. Ürmössy, *Eur. Phys. J. A* **40**, 325 (2009).
- [7] T.S. Biró, *Eur. Phys. J. A* **40**, 255 (2009).
- [8] W.M. Alberico, A. Lavagno, *Eur. Phys. J. A* **40**, 313 (2009).
- [9] G. Wilk, Z. Włodarczyk, *Eur. Phys. J. A* **40**, 299 (2009).
- [10] H. Zheng, L.L. Zhu, *Adv. High Energy Phys.* **2016**, 9632126 (2016).
- [11] E. Schnedermann, J. Sollfrank, U. Heinz, *Phys. Rev. C* **48**, 2462 (1993).
- [12] ALICE Collaboration (J. Adam *et al.*), *Phys. Rev. C* **93**, 024917 (2015).
- [13] T. Bhattacharyya, J. Cleymans, A. Khuntia, P. Pareek, R. Sahoo, *Eur. Phys. J. A* **52**, 30 (2016).
- [14] D. Thakur, S. Tripathy, P. Garg, R. Sahoo, J. Cleymans, *Adv. High Energy Phys.* **2016**, 4149352 (2016).
- [15] H.-R. Wei, F.-H. Liu, R.A. Lacey, *Eur. Phys. J. A* **52**, 102 (2016).
- [16] H.-L. Lao, H.-R. Wei, F.-H. Liu, R.A. Lacey, *Eur. Phys. J. A* **52**, 203 (2016).
- [17] H.-R. Wei, F.-H. Liu, R.A. Lacey, *J. Phys. G* **43**, 125102 (2016).
- [18] S. Takeuchi, K. Murase, T. Hirano, P. Huovinen, Y. Nara, *Phys. Rev. C* **92**, 044907 (2015).
- [19] H. Heiselberg, A.M. Levy, *Phys. Rev. C* **59**, 2716 (1999).
- [20] PHENIX Collaboration (S.S. Adler *et al.*), *Phys. Rev. C* **69**, 034909 (2004).
- [21] For the STAR collaboration (V. Bairathi), *Nucl. Phys. A* **956**, 292 (2015).
- [22] STAR Collaboration (B.I. Abelev *et al.*), *Phys. Rev. C* **79**, 034909 (2009).
- [23] PHENIX Collaboration (K. Adcox *et al.*), *Phys. Rev. C* **69**, 024904 (2004).
- [24] PHENIX Collaboration (K. Adcox *et al.*), *Phys. Rev. Lett.* **88**, 242301 (2002).
- [25] For the PHENIX Collaboration (T. Chujo), *Nucl. Phys. A* **715**, 151 (2003).
- [26] For the PHENIX Collaboration (T. Chujo), *Nucl. Phys. A* **721**, 273 (2003).
- [27] PHENIX Collaboration (K. Adcox *et al.*), *Nucl. Phys. A* **757**, 184 (2005).
- [28] A. Kiyomichi, *Study of identified hadron spectra and yields at mid-rapidity in $\sqrt{s_{NN}} = 200$ GeV Au+Au Collisions* (Ph.D. thesis, University of Tsukuba, Japan, 2005).
- [29] M. Vasileiou, *EPJ Web of Conferences* **126**, 04052 (2016); ALICE Collaboration (B. Abelev *et al.*), *Phys. Lett. B* **736**, 196 (2014).
- [30] R. Odorico, *Phys. Lett. B* **118**, 151 (1982).
- [31] UA1 Collaboration (G. Arnison *et al.*), *Phys. Lett. B* **118**, 167 (1982).
- [32] M. Biyajima, T. Mizoguchi, N. Suzuki, arXiv:1604.01264 (2016).
- [33] Z.B. Tang, Y.C. Xu, L.J. Ruan, G. van Buren, F.Q. Wang, Z.B. Xu, *Phys. Rev. C* **79**, 051901(R) (2009).
- [34] X.N. Wang, M. Gyulassy, *Phys. Rev. Lett.* **86**, 3496 (2001).
- [35] D. Kharzeev, M. Nardi, *Phys. Lett. B* **507**, 121 (2001).
- [36] A.N. Mishra, R. Sahoo, P. Sahoo, P. Pareek, N.K. Bhera, B.K. Nandi, *Eur. Phys. J. A* **52**, 319 (2016).
- [37] L. Zhou, G.S.F. Stephans, *Phys. Rev. C* **90**, 014902 (2014).